Mantle Deformation Processes during the Rift-to-Drift Transition at Magma-Poor Margins

Nicholas J. Montiel[1], Emmanuel Masini[2], Luc Lavier[3], Othmar Müntener[4], and Sylvain Calassou[5]

[1]University of Texas Institute for Geophysics.

[2]M&U France, Grenoble.

[3]University of Texas Institute for Geophysics.

[4]University of Lausanne.

[5]R&D Total Energies.

Corresponding author: Nicholas J. Montiel (nmontiel@utexas.edu)

Key Points:

- Large shear zones in the sub-continental mantle accommodate depth-dependent thinning of the lithosphere and upwelling asthenosphere.
- Anastomosing shear zone networks in the mantle control the structure of the ocean-continent transition.
- Buoyant, melt-rich mantle alters the stress environment of continental rifts and causes a reversal in fault orientation.

Abstract

The rift-to-drift transition at rifted margins is an area of active investigation due to unresolved issues of the ocean-continent transition (OCT). Deep structures that characterize modern OCTs are often difficult to identify by seismic observations, while terrestrial exposures are preserved in fragments separated by tectonic discontinuities. Numerical modeling is a powerful method for contextualizing observations within rifted margin evolution. In this article, we synthesize geological observations from fossil ocean-continent transitions preserved in ophiolites, a recent seismic experiment on the Ivorian Margin of West Africa, and GeoFLAC models to characterize mantle deformation and melt production for magma-poor margins. Across varied surface heat fluxes, mantle potential temperatures, and extension rates our model results show important homologies with geological observations. We propose that the development of large shear zones in the mantle, melt infiltration, grain size reduction, and anastomosing detachment faults control the structure of OCTs. We also infer through changes in fault orientation that upwelling, melt-rich asthenosphere is an important control on the local stress environment. During the exhumation phase of rifting, continentward-dipping shear zones couple with seaward-dipping detachment faults to exhume the subcontinental and formerly asthenospheric mantle. The mantle forms into core-complex-like domes of peridotite at or near the surface. The faults that exhume these peridotite bodies are largely anastomosing and exhibit magmatic accretion in their footwalls. A combination of magmatic accretion and volcanic activity derived from the shallow melt region constructs the oceanic lithosphere in the footwalls of the out-of-sequence, continentward-dipping detachment faults in the oceanic crust and subcontinental mantle.

Plain Language Summary

When continents break-up and create oceanic lithosphere in between, the resultant transition zone between the continental and oceanic crust is an area of active investigation. These areas are difficult to study because they're often underwater or they're only partially preserved where continentents have collided. Since the mantle is the strongest part of the lithosphere, understanding what kinds of deformation processes are taking place is important for understanding how the transition between continental lithosphere and oceanic lithosphere comes about. We combine previous studies of fragmentary transition zones with newly published seismic images of the transition zone off the Ivory Coast with computer simulations to understand how the mantle behaves during rifting. We come to three major conclusions: 1) large shear zones in the mantle are important for thinning the lithosphere, 2) the transition between continent and ocean is marked by complex, braided-looking faults, and 3) the upward push from magma in the mantle changes how faults are shaped when the oceanic lithosphere begins to form.

1 Introduction

How the mantle lithosphere deforms during rifting remains one of the most debated issues in plate tectonics. However, two mechanisms that complement each other are preferred by the community. These are the magma assisted diking or weakening of the mantle (Buck, 2006; Piccardo et al., 2007) and depth-dependent thinning (DDT) (Huismans & Beaumont, 2011; Huismans & Beaumont, 2008, 2014; Kusznir et al., 2005; Lavier et al., 2019; Royden & Keen, 1980). DDT is the process by which the mantle lithosphere initially thins passively and weakens through the localization of deformation along lithosphere-scale shear zones and the upwelling of a buoyant mantle (Huismans & Beaumont, 2011). This latter mechanism is preferred for magma

poor margins where little volcanism is expressed at the rift surface before the transition to oceanic crust. Observations of exhumed or denuded mantle lithosphere in the southern European Alps (Lanzo peridotite) show that melt migration through porous mantle lithosphere at depths between 50 and 15 km can also weaken the mantle by reducing viscosity (Kaczmarek & Müntener, 2008; Piccardo et al., 2007) and likely lead to DDT (Huismans & Beaumont, 2011; Lavier et al., 2019; Ros et al., 2017; Svartman Dias et al., 2015). The mantle lithosphere in this model thins and delaminates, reducing the lithosphere's yield stress and allowing the continental rift to split the lithosphere into two plates (Davis & Kusznir, 2016; Svartman Dias et al., 2015, 2016). This mode of rifting is supported by both global surveys of crustal and lithospheric thinning factors (Kusznir & Karner, 2007) and numerical models of magma-poor rifted margins (e.g., Huismans and Beaumont, 2011, Ros et al., 2017; Lavier et al., 2019). In this article, we address interactions between mantle deformation and magmatic processes that control magma-poor rifted margin evolution, focusing on the rift-to-drift transition using field geological evidence, seismic imaging, and numerical modeling.

Despite the rich literature on fossil rifted margins, progress on this issue requires further observations to spatially link (both in depth and along the OCT) structures and magmatic emplacements prior to the establishment of a stable seafloor spreading center. One locality that can provide these observations is the Deep Ivory Coast Basin (DICB; also referred to as the Ivorian margin or Deep Ivorian Basin) rifted margin off West Africa. The DICB is a small magma-poor margin situated between two transform margins associated with the St. Paul and Romanche Transform Zones (Basile et al., 1993; Mascle & Blarez, 1987). The DICB has recently been the subject of a high-resolution, 3D seismic experiment, making it a convenient natural laboratory for studying the whole rift-to-drift transition. In this paper we interpret seismic sections from the Ivory Coast margin that clarifies the mechanisms controlling the transition from rift to drift. In addition, we test our hypotheses using numerical experiments simulating lithospheric extension with boundary and initial conditions consistent with magma-poor margins. Because modern rifts and preserved rifted margins only preserve snapshots or end-states of rifted margin evolution, numerical models are crucial for understanding how these systems evolve through time and *in situ*.

1.1 Mantle deformation processes

Slow and ultra-slow spreading at mid ocean ridges provide a window into mantle deformation processes. At first order, core-complexes exhume mantle to the ocean floor along large-offset normal faults (Cann et al., 1997; Tucholke et al., 1998). These detachment structures form through weakening by serpentinization and melt infiltration of abyssal peridotites that facilitate the large amount of extension needed to bring mantle lithosphere from ~10-15 km depth to the surface (Escartín et al., 2001). More recent work in the Southwest Indian Ridge (SWIR) and in Western Alpine ophiolites shows that other weakening mechanisms such as dynamic grain recrystallization and melt infiltration may also control the formation of detachment faults in the mantle (e.g., Kaczmarek & Müntener, 2008; Linckens et al., 2011; Warren & Hirth, 2006). Similarly, at continental rifts, magma-poor margins experience a phase of mantle exhumation preceding seafloor spreading initiation (Franke, 2013; Manatschal, 2004; Peron-Pinvidic et al., 2013; Tugend et al., 2018; Boillot et al.,1989).

Seismic reflection and refraction experiments at the Newfoundland-Iberian conjugate margins show large domains (in excess of 50 km) of exhumed mantle (McIntosh et al., 2013; Pedrera et

al., 2017; van Avendonk et al., 2006, 2009). This is also observed at magma-poor margins in the Angola-Gabon margin, East India margin, and Australia-Antarctica conjugate margins (Gillard et al., 2013; Harkin et al., 2019; Peron-Pinvidic et al., 2013, McCarthy et al. 2020). Drilling and dredging in Iberia and Newfoundland have confirmed the presence of peridotite and serpentinite (Boillot et al., 1987; Manatschal et al., 2007). Overall, the character of magma-poor margins is that of exhumed or denuded mantle in along oceanic core-complex-like structures and a limited amount of volcanic activity prior to seafloor spreading initiation (Franke, 2013; Peron-Pinvidic et al., 2013; Tugend et al., 2018) (Fig. 1). Understanding the dynamics and kinematics of the mantle lithosphere, which makes up the bulk of lithospheric strength (Buck, 2006), is therefore fundamental to understanding extensional tectonics. While there is a fair amount of evidence for mantle exhumation, the transition from mantle exhumation to seafloor spreading at magma-poor margins is still poorly constrained and leads to the broad use of "ocean-continent transition" (OCT) or "continent-ocean transition" (COT) to characterize this key domain for addressing breakup processes and the birth of a Mid Oceanic Ridge. For example, at the Newfoundland-Iberia conjugate margins, the transition is highly controversial due to differing interpretations of a strong magnetic anomaly, which may or may not represent a sharp or diffuse boundary between lithospheric necking and seafloor spreading (Bronner et al., 2011; Nirrengarten et al., 2017, 2018). Similar debates surround the East Coast Magnetic Anomaly (ECMA) and the Blake Spur Magnetic Anomaly (BSMA) of the Eastern North American rifted margin (Biari et al., 2021; Shuck et al., 2019). Whether or not these magnetic anomalies represent paleomagnetic isochrons or whether they are magma bodies generated by another, earlier, ultimate rifting process has important implications for characterizing the rift-to-drift transition.

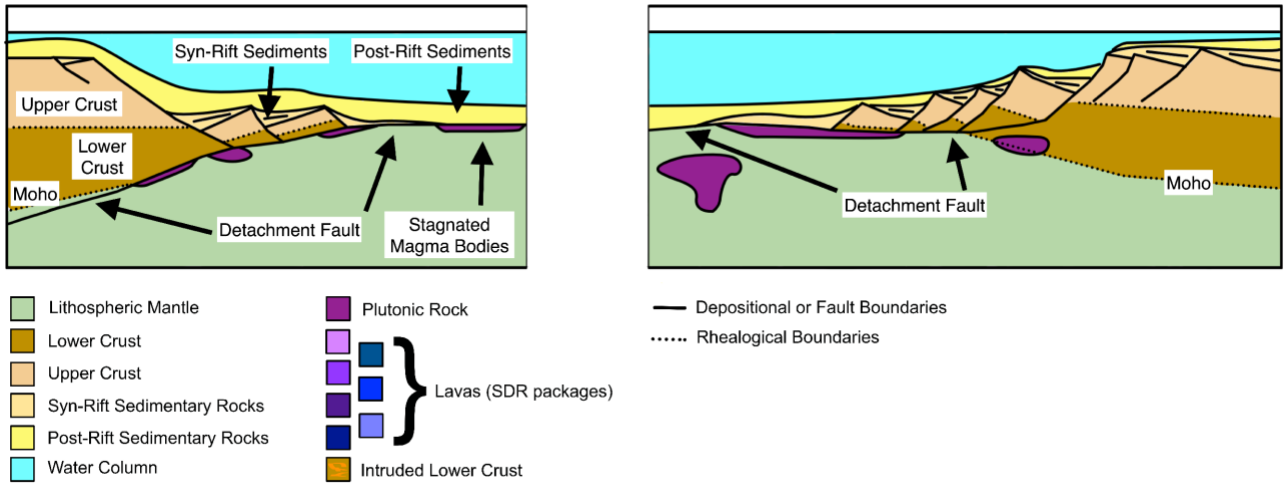

Figure 1. The classical view of lava-poor rifted margin (magma-poor or non-volcanic in other literature) as typified by previous interpretations of the Alpine-Tethys paleomargin, the Iberia-Newfoundland margins, and elsewhere in the Atlantic, Arctic, Indian Oceans and Antartic-Australian margins (e.g., Franke, 2013; Tugend et al., 2019, McCarthy et al. 2020). Lava-poor margins are characterized by an absence of seaward dipping reflectors (SDRs), seaward dipping normal faults along the rift flanks, exhumation of the lower crust and mantle by low-angle detachment faults, and structural asymmetry between conjugate margins. While volcanism is not as widespread as at volcanic margins, it is not absent or even rare in lava-poor settings except in the end-member case of the Iberia-Newfoundland margin. Magma bodies form in the mantle and

lower crust in the lead up to seafloor spreading, but are not expressed at the surface as 5-15 km thick SDRs

Serpentinization has been invoked as a weakening mechanism to explain lithospheric rupture at magma-poor margins for temperature and depth conditions of less than 350ºC and less than 15 km (Lavier & Manatschal, 2006; Pérez-Gussinyé & Reston, 2001, Gillard et al. 2019). As subcontinental mantle and former asthenospheric mantle are brought near to or at the surface by detachment faults, serpentinization reactions transform the shallow rheology of the lithosphere. Serpentinite is weaker than peridotite (Escartin et al., 2001) and may allow for enhanced detachment faulting while also acting as a "seal" that prevents melt migration (and fluid migration more generally) once the fault shuts off (Skelton et al., 2005). In a well preserved ocean-continent transition in the Eastern Central Alps, the hydration of detachment faults and the conversion of peridotite to serpentinite or serpentine cataclasite in the fault gouge suggests that serpentinization is a potential weakening mechanism during extensional tectonics (Manatschal et al., 2007, Gillard et al. 2019). However, studies of serpentinized mantle exposed at the Newfoundland-Iberia conjugate margins point towards serpentinization having an insufficient effect to rupture the lithosphere to initiate seafloor spreading. Pre-seafloor-spreading magmatism (manifested as the J magnetic anomaly) was widespread even as serpentinized mantle was exhumed over >50 km, which is difficult to reconcile with a regime in which serpentinization incites final break-up (Nirrengarten et al., 2017).

In the Alpine, Pyrenean, and Uralide orogens, fossil margins preserve evidence of mantle exhumation along detachment faults and offer hints of the processes governing the deformation of the mantle lithosphere. The Err-Platta ophiolite represents a shallow domain of rifted margins where extension brought mantle rocks into contact with surficial sedimentary rocks (Manatschal & Nievergelt, 1997; Schaltegger et al., 2002). The Lanzo Massif also preserves a section of an Alpine-Tethyan magma-poor margin, specifically the intra-mantle structures associated with extension, (Fig. 2a). The Lanzo detachment fault system forms a network of anastomosing shear zones, visible from patterns of foliation in Fig. 2a and represented in 3-D in Fig. 2b. Enrichment of incompatible elements associated with the shear zone of this detachment suggest that it was a conduit for melt migration (Kaczmarek & Müntener, 2010 (Fig. 2c). This is consistent with observations in other core complexes, such as the Cemetery Ridge continental-core complex in Arizona where Miocene igneous bodies intrude into the detachment fault system (Seymour et al., 2018; Strickland et al., 2018) as well as with geothermal activity at oceanic core-complexes (Blackman et al., 2011; Harding et al., 2017; Hayman et al., 2011; Zhao et al., 2013). This melt percolation at high temperature weakens faults, shear zones, and the lithosphere as a whole and may prove to be a powerful weakening mechanism to explain lithospheric rupture and final beak-up before seafloor spreading initiates (e.g., Müntener & Piccardo, 2003; Piccardo et al., 2007).

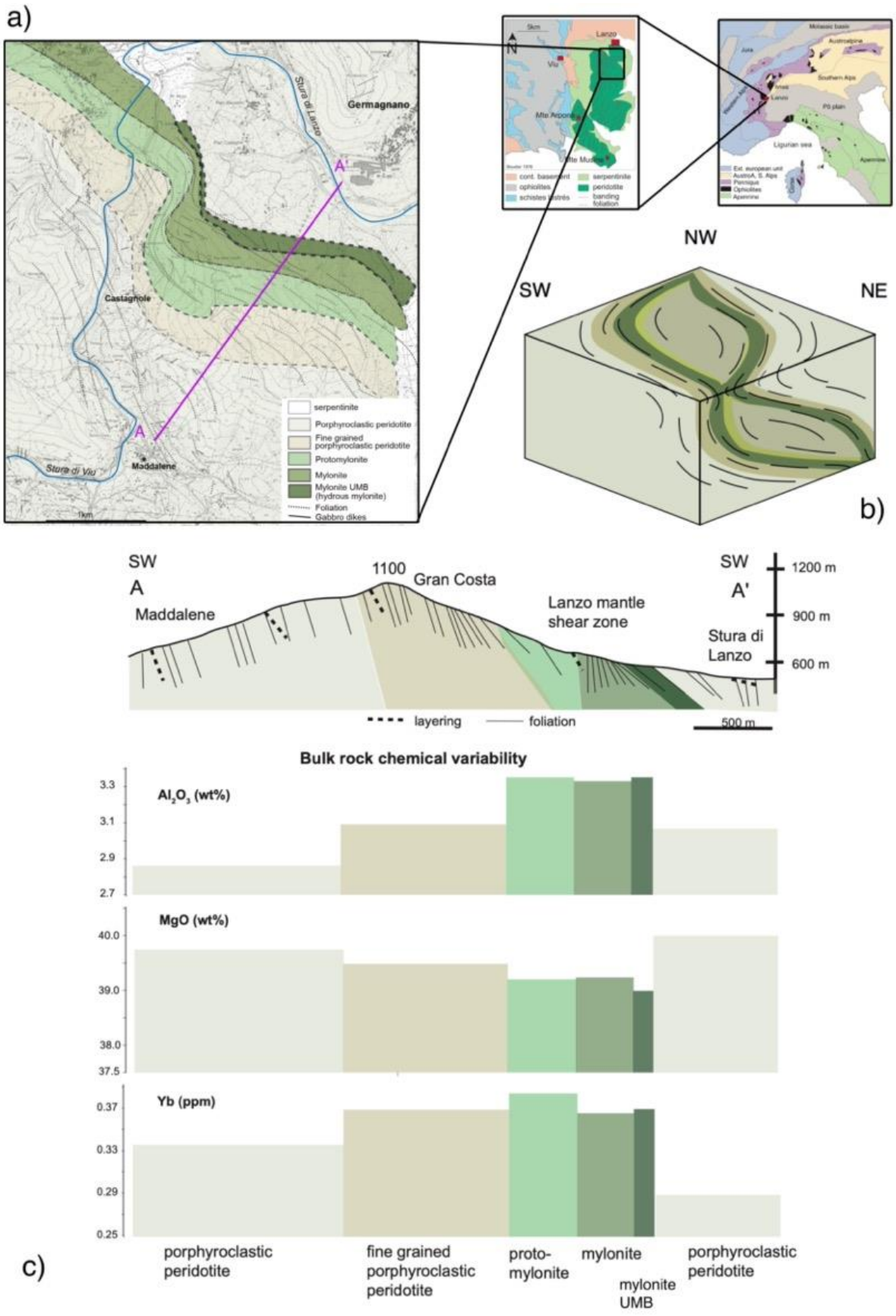
a)
Germagnano
Stura di Lanzo
Castagnole
Maddalene
Stura di Viù
A
A'
1km
serpentinite
Porphyroclastic peridotite
Fine grained porphyroclastic peridotite
Protomylonite
Mylonite
Mylonite UMB (hydrous mylonite)
Foliation
Gabbro dikes
Lanzo
Viù
Mte Arpone
Mte Musiné
5km
cont. basement
ophiolites
schistes lustrés
serpentinite
peridotite
banding
foliation
Molasic basin
Austroalpine
Southern Alps
Lanzo
Po plain
Ligurian sea
Apennine
Ext. european unit
Austroal. S. Alps
Pennique
Ophiolites
Apennine
NW
SW
NE
b)
SW
A
Maddalene
1100
Gran Costa
Lanzo mantle shear zone
SW
A'
Stura di Lanzo
1200 m
900 m
600 m
layering
foliation
500 m
Bulk rock chemical variability
Al2O3 (wt%)
3.3
3.1
2.9
2.7
MgO (wt%)
40.0
39.0
38.0
37.5
Yb (ppm)
0.37
0.33
0.29
0.25
porphyroclastic peridotite
fine grained porphyroclastic peridotite
proto-mylonite
mylonite
mylonite UMB
porphyroclastic peridotite
c)

Figure 2. a) Geological map of the northeastern part of the Lanzo Massif peridotite body, including context within the Western Alps. The northern region of Lanzo features a progression of peridotite textures from proto-granular,, porphyroclastic, proto- mylonite, to mylonite that mark the evolution of a detachment fault dipping towards the northeast. The hanging-wall of this detachment fault has proto-granular textures. Having a detachment fault with sheared mylonites below it and relatively undeformed rocks above is diagnostic of metamorphic core-complex style extension (e.g., Davis, 1983). Foliation in the mylonite shear zone shows sigmoidal trends that are most prominent near the detachment fault which indicates an anastomosing detachment fault and shear zones. **b)** 3-D- model of the anastomosing detachment faults and shear zones based on the mapped foliation within the Lanzo Massif peridotite. **c)** A cross section of the Lanzo Massif with aluminum silicate, magnesium oxide, and ytterbium content as a function of textural units. Within the mylonites and proto-mylonites, aluminum oxide and Yb concentrations rise to 32.5-34 wt% and 0.35-0.38 ppm, respectively, while the magnesium oxide concentrations drop to 39.0-39.3 wt%. In the proto-granulite of the foot wall, magnesium oxide has a concentration of 39.7 wt% compared to 41 wt% in the hanging wall. The Yb concentration in the proto-granulite between the foot wall and hanging wall also changes, from 0.33 to 0.28 ppm. The variability implies the refertilization of the shear zone by melt moving through it as well as higher temperatures and melt concentration in the peridotite that composes the foot wall. Figure is modified from Kaczmarek & Müntener (2010) and from Vieira Duarte et al., (2020).

The Nurali Massif in the Urals echoes the findings of the Lanzo Massif. Nurali is a peridotite body which is part of an ophiolite complex bounded on the west by the Main Uralian Fault and on the east by gabbros and a serpentinized tectonic mélange. This system of ophiolites was emplaced during the Uralide orogeny and preserves the rifted margin of the Paleo-Uralian Ocean (Puchkov, 2009; Spadea et al., 2003).. Throughout the peridotite, sigmoidal patterns of foliation suggest the presence of anastomosing shear zones. The foliation in the dunite and gabbro units dip steeply (~80º) westward towards where the Paleo-Uralian coastline would have been. REE and LREE analysis suggests fertilization by MORB-like melts. The easternmost domain of the preserved Nurali rifted margin is often cut by continent-dipping (with respect to the paleogeography) faults. A favored interpretation of the Nurali massif ophiolite is of a continent-ocean transition from the opening of the Paleo-Uralian Ocean, where the transition from peridotite to gabbro represents the transition from sub-continental mantle to oceanic crust (Spadea et al., 2003).

One key weakening mechanism implicated at Lanzo and Nurali is dynamic grain recrystallization. Analysis of deformed mineral grains within the anastomosing shear zone at Lanzo shows evidence of chemical disequilibrium and decreasing grain size with degree of deformation, suggesting that high-temperature deformation and melt infiltration were happening simultaneously, with melt-rock interactions and grain recrystallization causing localization of deformation (Higgie & Tomasi, 2014; Kaczmarek & Müntener, 2008; Müntener & Piccardo, 2003). This mechanism is also prevalent at modern slow spreading ridges, such as the SWIR (Bickert et al., 2021) and suggest that it plays an important role in determining the deformation processes in the mantle lithosphere under magma-poor conditions. Recent work by Ruh et al. (2021) showed that lithospheric-scale shear zones, in which diffusion creep is dominant and grain size reaches down 100 μm, reduce lithospheric strength and dominates tectonic deformation. They used a paleowattmeter to calculate grain size (Austin & Evans, 2007). Viscosity was obtained by calculating the geometric average of diffusion and dislocation creep

and by using the slow rate of grain growth on the order of millions of years given by (Speciale et al., 2020). Here we approach the same process using the work of Bickert et al. (2020) that provides an additional constraint to the onset of DRX at high temperature in the mantle lithosphere. DRX initiates for a given critical strain for a given temperature and strain rate condition in a wide range of materials (Jonas & Poliak, 2003; Poliak & Jonas, 1996; Sakai et al., 2014). Materials undergoing dynamic grain recrystallization first undergo a phase of hardening until a maximum stress is reached after which strain softening occurs (Cho et al., 2019; Sakai et al., 2014). This phenomenon is observed for DRX in olivine at various strain rates and temperatures (Hansen et al., 2012). In order to simulate the onset of DRX in a mantle lithosphere primarily composed of dry olivine deforming by dislocation creep we chose the approach of Poliak and Jonas (1996) which states that DRX occurs for a critical energy threshold, E_c corresponding to a critical stress, σ_c for a range of strain rate, $\dot{\varepsilon_{II}}$, $\sigma_c \dot{\varepsilon_{II}} > E_c$ ($\dot{\varepsilon_{II}}$ is the square root of the second invariant of the strain rate tensor or effective strain rate). This critical condition occurs when the amount of tectonic work provided is equal to the rate of irreversible deformation in the olivine crystal. Here we assume that the critical stress corresponds to an effective stress of 200 MPa estimated from recrystallized grain sizes in shear zone samples from the SWIR (Bickert et al., 2021; Bickert et al., 2020). We chose an effective strain rate of 10^{-14} s^{-1} to match long term tectonic evolution rates of deformation. This is a crucial assumption as localization in lithospheric scale mantle shear zone will control the strength and weakening of the mantle lithosphere.

2 Ivorian OCT imaged by reflection seismic data

2.1 Geological context

The Ivorian (or DICB) rifted margin and its Brazilian Para-Maranhao conjugate formed as one of the Equatorial Atlantic pull-apart rift segments formed between separating Africa and South America at Cretaceous times. It formed between the Saint Paul and Romanche transforms located respectively north and South of the present-day DICB (Fig. 3a). Rifting started in the early Barremian (~131 Ma) and lasted until the Late Albian when lithospheric breakup occurred separating the DICB from the Para-Maranhao rift basins with the Equatorial Atlantic oceanic crust (Blarez, E. & Mascle,1988; Basile et al., 1993, 2005; Labails et al., 2010; Moulin et al., 2010; Gillard et al; 2019). From this time onwards, post-rift sedimentation passively sealed the DICB ocean-continent transition imaged by both seismic reflection and field method data we use in this study (magnetic and gravity anomaly from www.geomapapp.org / CC BY, Ryan et al., 2009, Fig. 3b & 3c).

Depth-migrated seismic reflection data of the Ivory Coast reveal a non-overprinted ocean-continent transition in high resolution and in three dimensions. The area of study provides a coverage from the tip of the thinned continental crust to the first tabular oceanic crust from proximal to distal (Fig 3). It is noteworthy that this OCT was reported to be magma-poor by Gillard et al. (2019) who proposed it is formed by a “hybrid” crust made of exhumed mantle rocks overprinted by subsequent magmatic additions. Here we further use a 3D seismic dataset to characterize the spatio-temporal interaction between extensional tectonics and magmatism transitionally leading to steady-state seafloor spreading.

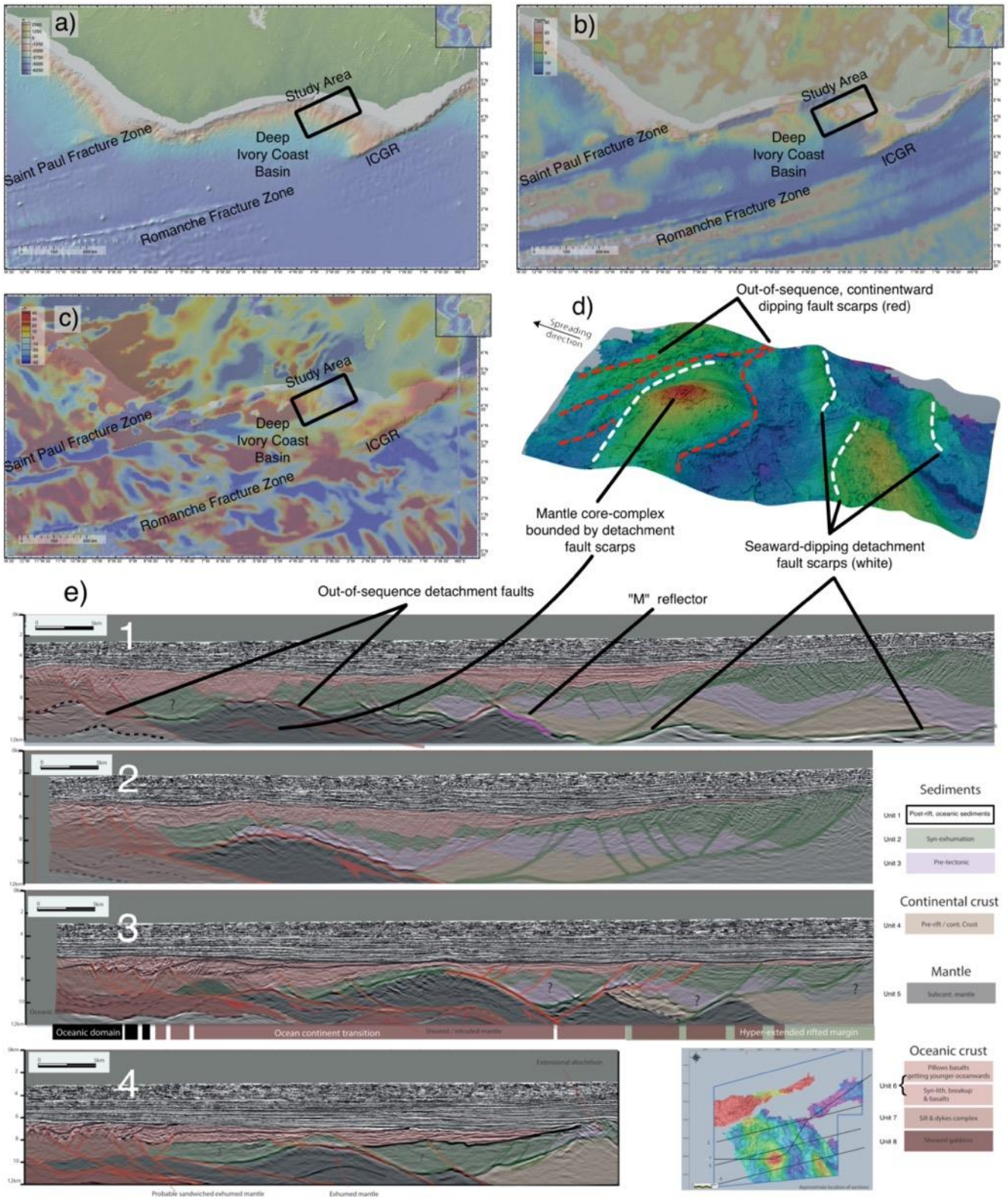
a)
Study Area
Saint Paul Fracture Zone
Deep
Ivory Coast
Basin
ICGR
Romanche Fracture Zone
b)
Study Area
Saint Paul Fracture Zone
Deep
Ivory Coast
Basin
ICGR
Romanche Fracture Zone
c)
Study Area
Saint Paul Fracture Zone
Deep
Ivory Coast
Basin
ICGR
Romanche Fracture Zone
d)
Spreading direction
Out-of-sequence, continentward dipping fault scarps (red)
Mantle core-complex bounded by detachment fault scarps
Seaward-dipping detachment fault scarps (white)
e)
Out-of-sequence detachment faults
"M" reflector
1
2
3
4
Oceanic domain
Ocean continent transition
Hyperextended rifted margin
Probable sandwiched exhumed mantle
Exhumed mantle
Sediments
Unit 1
Post-rift, oceanic sediments
Unit 2
Syn-exhumation
Unit 3
Pre-tectonic
Continental crust
Unit 4
Pre-rift / cont. Crust
Mantle
Unit 5
Subcont. mantle
Oceanic crust
Unit 6
Pillows basalts getting younger oceanwards
Syn-lith. breakup &-basalts
Unit 7
Sill & dykes complex
Unit 8

265

Figure 3. Geological context and results for the Ivory Coast rifted margin seismic experiment. The three panels show **(a)** topographic, **(b)** free air anomaly, and **(c)** magnetic anomaly contexts for the Deep Ivory Coast Basin and the Ivorian rifted margin. The Ivorian rifted margin is a lava-poor situated between the two well- preserved transform margins associated with the Saint Paul and Romanche Fracture Zones offshore of the Ivory Coast and Ghana. The Romanche FZ produces the Ivory Coast-Ghanaian Ridge (ICGR) that bounds the Deep Ivory Coast Basin. The domed mantle is correlated to the westernmost 30 mgal free air anomaly in the study area. The onset of seafloor spreading is marked by a 40 nT magnetic anomaly to the west, as well. Made using GeoMapApp (www.geomapapp.org) / CC BY (Ryan et al., 2009). **d)** The base sediment horizon of the study area, characterized by the prominent dome in the spreading direction and positive, linear features landward. **e)** The four interpreted seismic profiles and their location within the study area. Except for Profile 1, which departs from a straight line to cross from the continental shelf to the denuded mantle dome to the incipient oceanic crust, each profile cuts straight across different parts of the Ivory Coast rifted margin. However, each section shows similar features: 1) continental crust and denuded mantle extended by seaward dipping detachment faults, 2) out-of-sequence detachment faults that further exhume the mantle to produce the characteristic dome, 3) increasing volcanism and magmatism in the seaward direction that eventually results in layered oceanic crust, and 4) anastomosing shear zones at the root of the out-of-sequence detachment faults that bring mantle intruded by igneous bodies near to the surface. A segment of the "M" reflector is labeled in Section 1 as a pink line.

2.2 Characterization

In this paper, we show 4 sections taken from the 3D seismic data located in the map in Fig. 3e as well as a 3D base sediment horizon (Fig. 3d). Continentward (i.e. on the western side), the base sediment horizon displays prominent, positive, linear topographic features proximal to the continent trending NNW-SSE. The seaward side of these features are characterized by scarps that show clear striations (or corrugations) trending in the direction of extension (WSW-ENE) and terminate into a rough, chaotic surface. This "floor" is marked by escarpments and its depth compared to the rest of the study area. Seaward (westward) of these features is a high, dome-like structure also covered by striations trending in the same direction (WSW-ENE). The continentward face of this dome is smooth, gently sloping, and corrugated parallel to the striations. On the seaward face of the dome, the slope is gentle but rough and lacks obvious striations. Note that a positive gravity anomaly in Fig. 3b is consistent with the location of the corrugated "dome." The most distal part of the top- basement surface is deep and hummocky, slightly shallower than the basement flooring the opposite side of the dome, and riven by escarpments trending NNE-SSW. Importantly, this last set of escarpments are not perpendicular to the spreading direction.

The 2D seismic sections crosscutting the surface further reveal the basin and crustal structure across the study area and show the transition between the hyperextended continental lithosphere and the oceanic lithosphere (Fig. 3e). The interpretation of the Ivory Coast seismic sections was done by distinguishing eight seismic units and 2 main set of faults as described below.

Unit 1 (transparent/white): This unit is characterized by thinly spaced, high amplitude, sigmoidal to parallel reflectors that are ubiquitous across the upper sections of each profile. Strata imaged in this seismic unit show clear onlap relationships above the units located below. This pattern of reflectors as mostly flat lying along with its position in the section, informs the

interpretation that this is a post-tectonic sedimentary depositional sequence made of continental slope and oceanic sediments.

Unit 2 (green): Unit 2 is characterized by thinly spaced, slightly diverging reflectors with varying dip angle that decrease in seismic amplitude with depth. Seismic reflectors display fan-shaped growth strata in association with seaward-dipping normal faults (as indicated by offset reflectors). Fan-shaped growth strata associated to normal fault in a domain where continental crust can be identified (see below) suggest this unit to be a syn-rift depositional sequence.

Unit 3 (purple): Characterized by a mix of chaotic reflectors and low amplitude, widely spaced complexly layered reflectors. Both sets of reflectors become fewer with increased depth. Due to the parallel lying stratigraphic reflections, this unit is interpreted to be pre-kinematic sedimentary layers in respect of the rift-related normal faults.

Unit 4 (light brown): This is characterized by a homogenous seismic facies with only some diffractions and chaotic reflectors in association with the lateral continuation of normal faults (shown by offsets in units or by bright reflectors). The fairly uniform features and position in relation to other units possibly indicates a crustal basement lithology.

Unit 5 (black): A unit with complex layering of high-amplitude reflectors and some regions with few to no reflectors. The upper boundary of this unit corresponding to the base of Unit 4 is a high-amplitude, thick reflector indicating a high impedance contrast referred to as the "M" reflector in this paper (mapped in 3D as the base sediment horizon). We propose the "M" reflector to be the continental Moho capping the subcontinental mantle corresponding to Unit 5. This interpretation is geometrically and isostatically consistent with a regional seaward rise of this reflector going along the deepening of the base sediment.

Unit 6 (light red): Characterized by wedge-shaped bodies of discontinuous, diverging reflectors mixed with chaotic reflectors, all of which vary in amplitude. We interpret them as syn-kinematic lava flows as reflections are shifted by normal faults (i.e. pillow basalts, hyaloclastites and/or basaltic breccias). They are observed on top of Unit 2 and Unit 7 where they correspond to the classical Layer 2a of Penrose type-oceanic crust (e.g., Cann, 1970; Nicolas 1989; Gómez-Romeu et al., 2022).

Unit 7 (medium red): A unit characterized by a seismic facies of low-amplitude reflectors. Because of its location below volcanic flows of Unit 6, we interpret this unit as sheeted mafic dikes equivalent to Layer 2b of Penrose type-oceanic crust (e.g., Cann, 1970; Nicolas 1989).

Unit 8 (dark red): This unit exhibits a similar characterization as Unit 5, but with the addition of sigmoidal reflectors interpreted to be sheared gabbros and other gabbroic bodies. The gabbroic bodies are in turn interpreted as intruding the mantle in a manner consistent with Gillard et al. (2019) and are part of a region equivalent to Layer 3 of Penrose-type oceanic crust (e.g., Cann, 1970; Nicolas 1989).

Distal margin detachment fault system (green): Faults defined by offsets in Units 2, 3, 4, and 5 that sole into the high-amplitude reflector atop the Unit 5 dome. This system's single decollement dips towards the ocean and recorded a top-to-the ocean senses of shear as shown by syn-rift wedging bounded by synthetic normal faults (generally dipping seaward as well) that are the shallow expressions of this system (exclusively found in the continentward part of the rifted margin).

Out-of-sequence detachment fault system (red): This system of faults offsets Units, 2, 3, 4, 5, 6, 7, and 8. It also crosscuts the distal margin detachment system and is therefore considered out-of- sequence with respect to this latter. These out-of-sequence faults are geometrically distinct, with high-angle normal faults locally soling into an extensional duplex that dips towards the continent. The duplex contains sigmoidal boudins of Units 5 and 8 bounded by anastomosing high-amplitude reflectors interpreted as shear zones.

2.3 Interpretation

Based on the seismic reflection images provided across the DICB, the Ivory Coast rifted margin records the transition from magma-poor continental rifting to seafloor spreading. Near the continent there is a seaward dipping, distal margin detachment faults system which bounds blocks of continental crust (extensional allochthon blocks), accommodates syn-rift basins above tapering continental crust and exhumes mantle further outboard. Towards the ocean basin, this set of faults are crosscut by out-of-sequence, continentward-dipping top-basement faults; anastomosing shear zones in the mantle; magmatism and volcanism; further exhumation of the mantle; and layered oceanic crust.

The earliest evidence of tectonic activity is the formation of the distal margin detachment system that accommodates the final extension of the continental and exhumes its underlying sub-continental mantle (Units 3, 4, and 5). The fanning reflectors in Unit 2 is indicative of growth structures and suggests that it's a syn-kinematic depositional system coeval with the earlier extensional phase in the area covered by the seismic survey (late rifting at the scale of the entire margin). The high-angle normal faults sole into a low-angle detachment fault with sub-continental mantle in its footwall. This is interpreted as relating to the ultimate tapering of the continental crust leading to mantle exhumation.

The second major phase of deformation is the development of an out-of-phase sequence of detachment faults with opposite vergence, hereby referred to as OCT detachment systems. The volcanic wedges of Unit 6 appear to be coeval with the shallow, high-angle faults associated with this set of faults. The seaward increase in Unit 6 thickness correlates to increased evidence of plutonic bodies in the mantle (Unit 8). Unlike distal margin detachment faulting, the OCT detachment system soles into multiple levels of decollement to form extensional duplexes. Blocks within these duplexes contain sub-continental mantle while the footwall of the whole system contains mantle material with sigmoidal reflectors interpreted to be sheared gabbroic bodies (similar to anastomosing shear zones at Lanzo, Nurali, and elsewhere). These gabbroic bodies increase in frequency and thickness in the seaward direction until they form Unit 8.

Unit 8 is the lowermost unit of the oceanic crust pseudo-stratigraphy (Nicolas 1989) seen in the most distal parts of the seismic section. Atop the sheared gabbros (Unit 8) are the sheeted dikes identified by the lack of reflectors and the presence of diffractions (Unit 7) and the pillow basalts and volcanics indicated by the mix of chaotic and divergent reflectors (Unit 6). These three units are Layers 3, 2b, and 2a of oceanic crust (Nicolas 1989). Layer 1, oceanic sediments, is represented by Unit 1, the most recent geologic unit in the study area.

3 Numerical modeling methods

3.1 Methods justification

While geological observations and seismic experiments provide observational constraints on rifted margin evolution, they are limited because they only provide snapshots of rifting stages.

Numerical modeling is necessary to link these localities in a spatio-temporal context to construct a framework for the evolution of a continental rift. The program GeoFLAC (FLAC stands for Fast Lagrangian Analysis of Continua) has been a useful tool for researchers for the past three decades by providing a means to explore the rheological, petrological, thermal, and kinematic evolution of rifting (Davis & Lavier, 2017; Detournay & Hart, 1999; Geoffroy et al., 2015; Poliakov et al., 1993). Recent work using geodynamic modelling purports to show that doming and exhumation of mantle peridotite via out-of- sequence detachments is the result of a "strength competition" between weak, frictional-plastic shear zones and thermal weakening beneath the necking domain of a continental rift (Theunissen & Huismans, 2022). Theunissen & Huismans (2022) also suggest that the mode of deformation is a consequence of varying extension rate and fault strength. Ruh et al. (2021) invoke dynamic grain recrystallization as a key process of lithospheric rupture in their own numerical modeling work. In this case, grain size reduction in olivine weakens the mantle lithosphere and allows for the formation of continentward-dipping shear zones. Our work can test these hypotheses by characterizing the roles that dynamic grain recrystallization, melt production and migration, and initial thermal conditions play in rifting.

3.2 Boundary conditions

All models presented here share initial geometries. The starting box is a two-dimensional slice of the lithosphere, 300 km wide and 150 km deep. The crustal thickness is initially 30 km for all models. To localize deformation in the center of the model space we impose thinning of the sub-continental mantle. Extensional velocity boundary conditions (1 or 2 cm./yr^{-1}) allow the box to extend passively until remeshing is needed and the box's width reset to 300 km. Remeshing occurs when the minimum angle in the triangular elements in the mesh drops below 15^{o}. The Winkler foundation and the addition of material during remeshing at the lower boundary allows for asthenosphere to be upwelled from below. The foundation simulates isostatic balance for each column of elements in the model box. The compensation depth is assumed to correspond to the bottom of the model box and the elastic, viscoelastic and plastic properties of the model simulate the regional isostatic response. The top boundary is free in both temperature and stress and the side boundaries experience no heat flow. The bottom boundary temperature is varying across the box as it is calculated using the adiabat geotherm for the asthenosphere (0.003^{o}C/km) (Davis & Lavier, 2017).

The boundary between the lithosphere and the asthenosphere is initially defined as the 1300ºC isotherm, though elements which subsequently cross the isotherm remain labeled as asthenosphere or lithosphere even as their rheology changes in response to temperature variations (this is necessary to visually demonstrate the provenance of mantle material during the exhumation and transition phases of rifting). Melt is produced by the method described by (Katz et al., 2003) based on anhydrous decompression melting of fertile mantle and adapted by Davis & Lavier (2017) for GeoFLAC. In the numerical experiments presented here we assume that for pre-rift conditions the mantle is anhydrous and is equivalent to normal mantle lherzolite, though we use the slightly damp solidus parameterized by Hirschmann et al. (2009). Once produced, melt moves with the solid mantle and is not extracted but recrystallizes when its temperature is below the solidus (Schmeling, 2010). When the melt crystalizes, the material in the element

undergoes a phase change that assigns the physical properties of plagioclase and olivine in proportions corresponding to the actual melt fraction in the particle.

The ten models were chosen to showcase a range of mantle potential temperatures from 1300ºC to 1400ºC, extension rates from 1 cm/yr to 2 cm/yr, and 45 mW/m^2 to 75 mW/m^2. From all those possible combinations of parameters, we chose the ones that exhibited homologous features to rifted margins and excluded models that failed to complete the rift-to-drift transition resulted in margins that were not reaching seafloor spreading or too melt-dominated to be considered magma-poor margins (> ~ 40% melt).

3.3 Rheological assumptions

In the crust, mantle lithosphere and asthenosphere we mainly use the same rheological assumptions as Lavier et al. (2019). To simulate the formation of ductile shear zones by dynamic recrystallization of olivine in the mantle lithosphere we use temperature and dissipation thresholds to initiate grain size reduction and viscous flow by diffusion creep (Bickert et al., 2020). This localization mechanism simulates the formation of high temperature anastomosing shear zones that are observed at Lanzo Massif, Nurali Massif, and elsewhere (e.g., Kaczmarek & Müntener, 2005; Kaczmarek & Müntener, 2010; Spadea et al., 2003). We use dislocation creep laws to calculate the deformation of mantle, crust, serpentinized mantle, weakened crust, basaltic crust, and sedimentary phases (Table 1) (Lavier et al., 2019). Localization of deformation in the brittle lithosphere is modeled by cohesion loss as a function of accumulated plastic strain in an elastoplastic material with a Mohr-Coulomb yield criterion (Lavier et al., 2000). The formation of ductile shear zones in the lower crust is achieved by simulating reaction or compositional weakening using a yield criterion with a work threshold dependent on both brittle (plastic) and ductile (dislocation creep) work (Lavier et al., 2019). This assumes that there always is a sufficient amount of meteoric or metamorphic fluids for a reaction to occur up to 15 km depth in the continental crust and 10 km depth for mantle serpentinization (Fricke et al., 1992). The work and temperature thresholds are given in Table 1.

Parameter	*Mantle*	*Serpentinized Mantle shear zones*	*Crust*	*Ductile shear zones in Crust*	*Basaltic Crust*	*Sediments*	*High temperature mantle shear zones*
Density (kg.m^{-3})	3300	3000	2800	2800	3000	2400-280	3300
Creep exponent, n	3	3	3	3	3.05	3	3
Creep pre-exponent (MPa^{-n}s^{-1})	7x10^{4}	1.25x10^{-1}	3x10^{-6}	5x10^{2}	1.25x10^{-1}	3x10^{-6}	3x10^{-6}
Creep Activation Energy (kJ.mol^{-1})	520	176	180	300	376	300	300
Friction angle (°)	30-15	5-5	30-15	5-1	30-15	30-15	5-1
Cohesion (MPa)	44-4	4-4	44-4	4-4	44-4	4-4	4-4
Lamé parameters (Pa)	3x10^{10}, 3x10^{10}	3x10^{10}, 3x10^{10}	3x10^{10}, 3x10^{10}	3x10^{10}, 3x10^{10}	3x10^{10}, 3x10^{10}	3x10^{10}, 3x10^{10}	3x10^{10}, 3x10^{10}
Work and Energy Thresholds (J)	5x10^{7} depth< 10 km, T<400°C		1x10^{7} depth< 15 km, 200<T<350°C				

Thermal Cond ($W.m^{-1}.K^{-1}$)	3.3	3.3	2.8	2.8	3.3	2.2	5

Table 1. Physical and rheological parameters used for the different types of material in the numerical models. Mantle and asthenosphere follow first a dislocation creep law for dry olivine before reaching a critical threshold at a diffusion creep, grain-size sensitive flow occurs. The olivine flow laws are from Hirth and Kohlstedt (2003). We assume that the oceanic crust is dominated by a plagioclase rheology given by Shelton and Tullis (1981) with a higher activation energy to make the oceanic crust stronger. For the continental crust, feldspar and wet quartz rheology are controlled by dislocation creep laws (Rybacki et al., 2008, 2010). The general equation for creep law is $\dot{\varepsilon} = A \cdot \sigma^n \cdot d^{-p} \exp\left(-\frac{Q}{RT}\right)$ with A the creep law pre-exponent that is determined experimentally ($\mu m^{-p} \cdot MPa^{-n} \cdot s^{-1}$); Q the activation energy (in $J.mol^{-1}$); n the stress exponent; p the grain size exponent in the diffusion creep law.

The formation of high temperature (>800°C) ductile shear zones in the mantle by dynamic recrystallization (DRX) is confirmed by petrological observations in oceanic core complexes (Warren and Hirth 2006, Bickert et al., 2021), in rifts in the Lanzo peridotite (Kaczmarek & Müntener, 2008), and potentially by the observation of earthquakes in the East African rift system and the southwest Indian ridge (SWIR) (Lindenfeld & Rümpker, 2011; Zhao et al., 2013). The onset of DRX and diffusion creep follows the approach discussed in the introduction. The recrystallized mantle (mantle2) is modeled as dry olivine and we use the diffusion creep, grain size-dependent rheology of (Hirth & Kohlstedt, 2003) (Table 1). When conditions of temperature and energy are appropriate, we use the Van der Wal et al. piezometer (Van der Wal et al., 1993) to calculate a recrystallized grain size from the local stress value (Bickert et al., 2020). We then calculate a new viscosity using the diffusion creep law. We delay the onset of DRX until 2 Myr to enhance localization of deformation in the center of the model space during the stretching phase of rifting. Erosion and sedimentation transport are modeled with a diffusive formulation and deposition is modeled a source term in the diffusion equation for sediments. Some transport of sediments occurs by the advection of the grid in the Lagrangian grid. The equation for sediment erosion is: $\frac{\partial h}{\partial t} = k \frac{\partial^2 h}{\partial x^2} + S_x$ where k is the diffusivity of the sediments in $m^2.s^{-1}$ and S_x (10^{-11} $m^2.s^{-1}$) is the source for the deposition of sediments, x is the horizontal direction and h the topography. Transport occurs as the numerical grids deform. k varies whether the sediments are under water ($k = 10^{-7}$ $m^2.s^{-1}$) or above sea-level ($k = 5x10^{-7}$ $m^2.s^{-1}$). If the sediments are below sea-level, they are water loaded and compacted following Atty's law for standard siliciclastic sediments (Allen & Allen, 2013). We did not vary the erosional parameters to study their effect on the thermomechanical evolution of the margin.

4 Numerical modeling results

We present nineteen models that possess homologous features with respect to observed magma-poor margins from both field geology and seismic experiments by varying mantle potential temperature (MPT); which controls LAB depth, surface heat flux (SHF), and extension rate. (Homologies are here defined as similarities between models and observations with respect to structure, composition, and spatio-temporal relations). All are relatively cold rifts with MPTs from 1300 to 1400ºC and SHFs from 45 to 75 $mW.m^{-2}$ (Table 2). For each model, we record the percentage of partial melting, oceanic lithosphere thickness (depth to the melt region), margin

widths, difference between conjugate flanks (asymmetry), number of lithospheric boudins, crustal boudins, and mantle boudins, the minimum and maximum length of boudins, the number of mantle core complexes, and the modal width of each model's anastomosing, extensional duplexes. The relationship between these observables and MPT, SHF, and extension rate are shown in Figs. S1-9, and the table of observed values is Table S1.

Surface Heat Flux (mW/m^2)	***Extension Rate (cm/yr)***	***Mantle Potential Temperature (ºC)***		
		1300	*1350*	*1400*
45	*1*	—	—	Model 7
55	*1*	Model 11	Model 12	Model 8
	2	Model 1	Model 13	Model 9
65	*1*	Model 2	Model 4	Model 14
	2	Model 3	Model 5	Model 10
75	*1*	Model 15	Model 6	Model 16
	2	Model 17	Model 18	Model 19

Table 2. The independent variables tested for each model presented in this study: surface heat flux, extension rate, and mantle potential temperature. "Hotter" cases with eleveated surface heat fluxes and mantle potential temperatures lie in the bottom right of the table, while "colder" cases lie in the top left. Empty cells are where rifts failed to form.

4.1 Model 1 case study

Model 1 is the primary model we will be examining in this study (Fig. 4). On both the phase and strain rate evolution image series we show six isotherms (1300ºC, 1100ºC, 800ºC, 450ºC, 300ºC and 150ºC). 1300ºC corresponds to the depth of the thermal lithosphere, 1100ºC the minimum temperature for the presence of melt in the lithosphere, 800ºC the minimum depth for the initiation of DRX, 450ºC the initial depth to Moho, 300ºC the average depth for the formation of ductile shear zones in the middle crust, and 150ºC the maximum temperature for the generation of hydrocarbons. The model shows most of the diagnostic features of magma-poor margins and the ocean-continent transition in detail. It therefore serves as a useful comparison to the Ivory Coast margin and to the Alpine Tethys and Uralide margins. The initial conditions of Model 1 **(0 Myr)** are a 1300ºC MPT, 55 $mW.m^{-2}$ SHF, and 2 $cm.yr^{-1}$ full extension rate. An imposed thinning of the lithosphere (compositional and thermal lithosphere) as a normal distribution with an amplitude of 10 km and a half width of 50 km localizes deformation in the center of the model. These initial conditions define a thermal anomaly located at the base of the lithosphere.

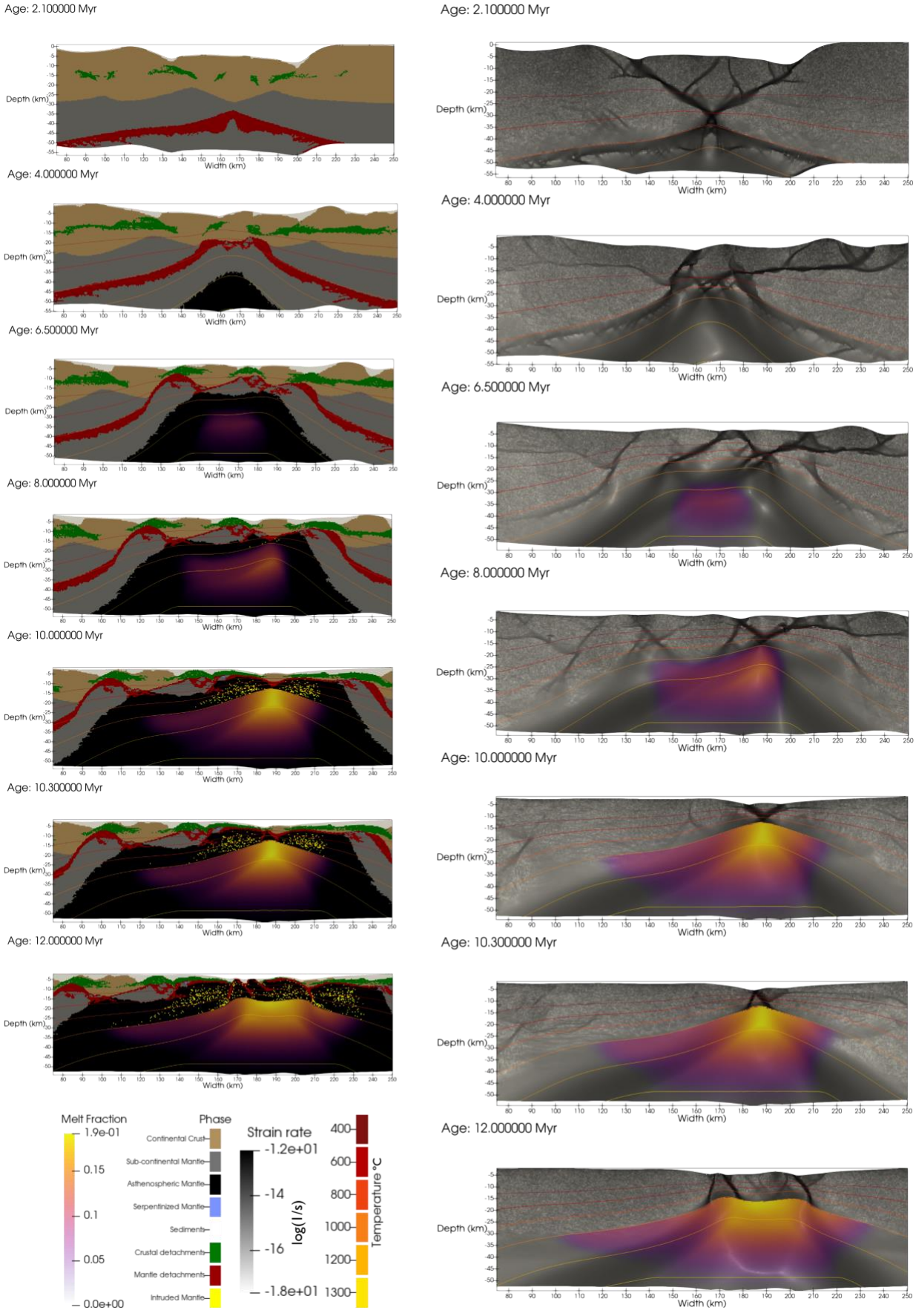
Age: 2.100000 Myr
Age: 4.000000 Myr
Age: 6.500000 Myr
Age: 8.000000 Myr
Age: 10.000000 Myr
Age: 10.300000 Myr
Age: 12.000000 Myr
Depth (km)
Width (km)
Melt Fraction
1.9e-01
0.15
0.1
0.05
0.0e+00
Phase
Continental Crust
Sub-continental Mantle
Asthenospheric Mantle
Serpentinized Mantle
Sediments
Crustal detachments
Mantle detachments
Intruded Mantle
Strain rate
-1.2e+01
-14
-16
-1.8e+01
log(1/s)
400
600
800
1000
1200
1300
Temperature °C

Figure 4. Key frames in the evolution of Model 1, with focus on lithology (left) or phase (right) strain-rate. **2.1 Myr:** localized crustal deformation and initiation of sub-continental mantle shear zones (necking phase). **4.0 Myr:** coupling between crustal detachment faults and the sub-continental mantle shear zones produces asymmetry in detachment faults and upwelling of the asthenosphere (exhumation phase begins). **6.5 Myr:** formation of mantle lithosphere boudins and doming; melt production matures and the 1300ºC isotherm ceases rising because of the latent heat of melting; out-of-sequence detachment faults initiate.. **8.0 Myr:** melt focuses underneath rift axis, "choosing" the site of future seafloor spreading. **10.0 Myr:** crustal detachment system shuts off except for the rift axis; percentage melt reaches highest value. **10.3 Myr:** new faults form with the opposite vergence; asthenosphere-derived material reaches the surface; seafloor spreading initiated. **12.0 Myr:** end-state of the model, producing oceanic crust. The waviness of the lower boundary is an artifact how our data visualization software extracts subsets and doesn't indicate anything meaningful. Isotherms for 400, 600, 800, 1000, 1200, and 1300 ºC are plotted from yellow to red.

At **1.0 Myr** distributed extension along high-angle normal faults (stretching phase) begins, as does the attenuation of the mantle lithosphere. This is particularly visible in figure 4b where zones of high strain rate ($>10^{-13}$ s^{-1}) mark the localization of high-angle normal faults in the crust, the initiation of H-block formation and mantle thinning (Lavier and Manatschal, 2006; Huismans and Beaumont, 2011; Lavier et al., 2019). After **2.1 Myr** crustal deformation becomes localized in an H-block with a 5 km thick root and sub- continental mantle shear zones (red shear zone dipping at ~ 20º) are initiated and accelerate mantle lithosphere attenuation. These shear zones form as a result of DRX being activated at 2 Myr. Subsequent deformation is characterized by the formation detachment faults rooted in low angle ductile shear zones in the middle crust. At **4.0 Myr** coupling between crustal detachment faults and the sub-continental mantle shear zones begins and produces of lithospheric scale detachment faults dipping at < 20 and upwelling of the asthenosphere to within < 30 km of the surface. At this stage the extension becomes highly asymmetric as is clearly seen in the strain rate and localized to the conjugate located on the right of the model. Rapid necking of the lithosphere is characteristic of magma- poor margins and observed in many models (Huismans and Beaumont, 2001, Svartman Dias et al., 2015; Ros et al., 2017; Lavier et al., 2019).

Starting at **5.7 Myr** melt production begins and the 1300ºC isotherm ceases to rise through transport because heat dissipation by latent heat of melting depresses the geotherms beneath the melt region. Between 4 and 5.7 Myr, out-of-sequence landward dipping detachment faults initiate in the crust and mantle with a tendency to dip landward and away from the rift axis. This lithospheric scale detachments are causing the formation of concave upward domes in the mantle underlying and thinning the crust locally down to 5 km. The high-temperature mantle shear zone forming by DRX generate a network of anastomosing shear zones. While deformation is more intense at the rift axis, a large 100 km wide horizontal detachment system connecting crustal normal faults and landward dipping high-temperature mantle shear zones is still active at the right flank of the rift. Reaching **6.5 Myr**, the mantle lithosphere continues to form domes and lithospheric boudins under the influence of the out-of-sequence detachment faults. Melt production reaches 6% and is focused on the rift axis. The asymmetry is active and deformation persists off axis.

At **8.0 Myr** the melt area (reaching 14% melt) displays some skewness as it is transported to the right of rift axis in contact with the crust (thinned to < 5km) and focuses deformation and uplift

beneath one of the crustal boudins that was previously formed. High temperature shear zones at the Moho depth laterally transport the subcontinental mantle to make space for the asthenospheric mantle that was initially located beneath the continent. The intensity of the deformation (strain rate) correspondingly increases at this site but remains distributed. The temperature structure at and below this crustal block (originating from the H-block) is following a pure shear model of deformation (McKenzie, 1978). The top of the thermal structure is at the seafloor at 10ºC while the base is located at the 1100ºC isotherm and Moho remains near 800ºC. The area of asthenospheric mantle bounded by the 800ºC and the 1100ºC isotherm (Min temperature for the presence of active melt) below the former rift axis delineates a new mantle lithosphere layer that expands through extensional processes occurring in the crust and denuded former mantle lithosphere.

At **10.0 Myr**: The crustal detachment system shuts off except for the rift axis; percentage melt reaches highest value of 19%. The crustal boudin is extruded by detachment structures originating in the high-temperature mantle and the mantle lithosphere thins by pure shear. Transport of melt across the solidus in the new mantle lithosphere layer generates pods of crystalized melt that are trapped in a new lithosphere formed by mechanical processes. 300 kyr later, at **10.3 Myr**, new high temperature mantle shear zones form with opposite vergence in the new asthenospheric layer; asthenosphere-derived material reaches the surface; pods of recrystallized melt continue forming in the asthenosphere and seafloor spreading initiated as deformation and melt production are fully localized. When the model reaches **12.0 Myr** oceanic lithosphere is formed by mantle core complexes and flip flop detachments rooted in high temperature mantle shear and weak recrystallized melt pods as in a very slow spreading environment (Bickert et al., 2020), homologous to what is seen as slow-spreading centers and seafloor spreading as described by Hess (Hess, 1962; Reston, 2018). However, the melt production area is expanding instead of being extruded by processes such as diking. A situation like that in our model may be possible only if DRX high temperature mantle shear zones become a barrier to melt migration.

4.2 All model results

The following are brief descriptions of each case with initial conditions outlined in Table 2 and shown in Figs. 5-7. Models are grouped by mantle potential temperature, then by extension rate, then by surface heat flux.

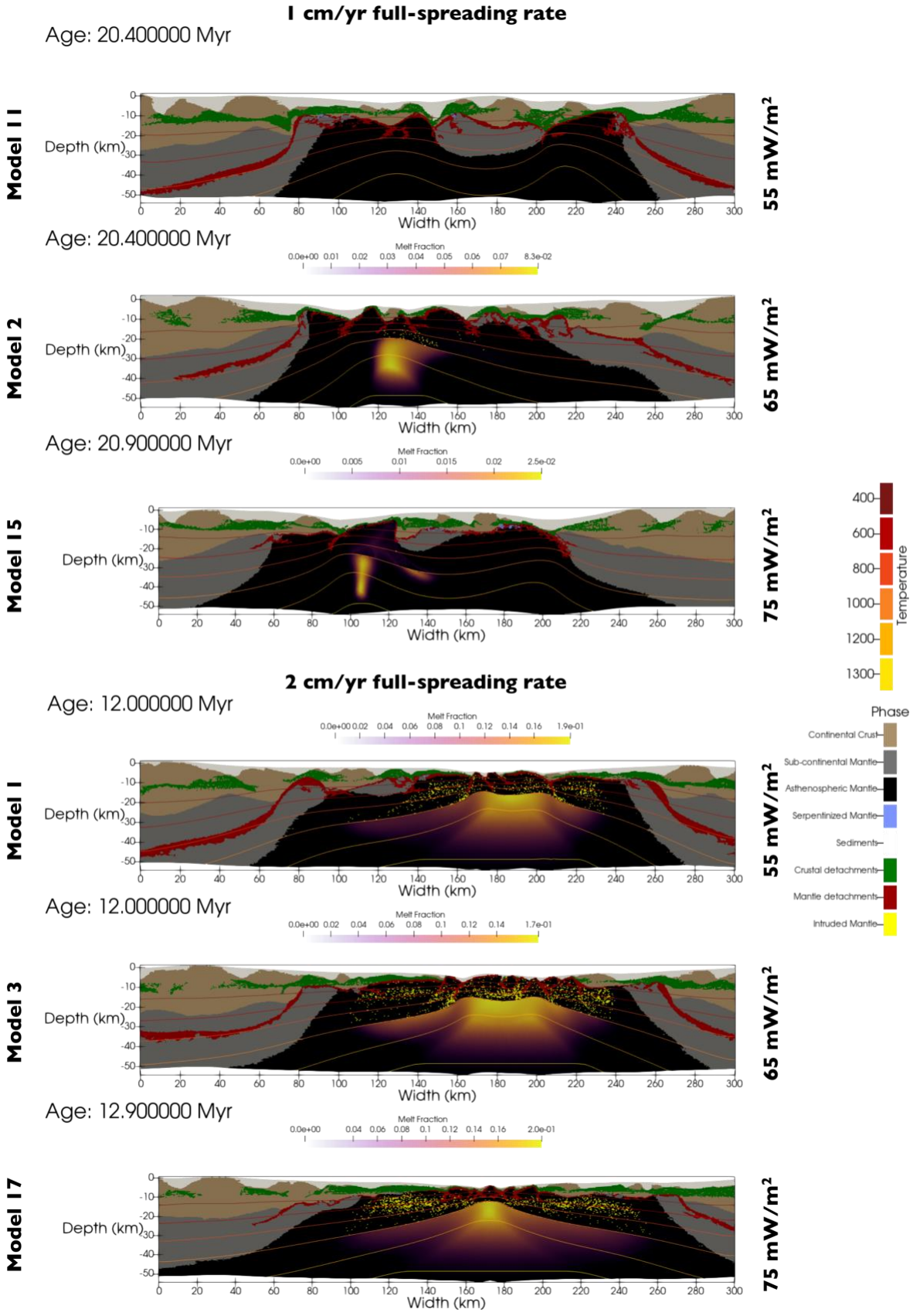
1 cm/yr full-spreading rate
Age: 20.400000 Myr
Model I 1
Depth (km)
Width (km)
55 mW/m²
Age: 20.400000 Myr
Melt Fraction
0.0e+00 0.01 0.02 0.03 0.04 0.05 0.06 0.07 8.3e-02
Model 2
65 mW/m²
Age: 20.900000 Myr
Melt Fraction
0.0e+00 0.005 0.01 0.015 0.02 2.5e-02
Model I5
75 mW/m²
2 cm/yr full-spreading rate
Age: 12.000000 Myr
Melt Fraction
0.0e+00 0.02 0.04 0.06 0.08 0.1 0.12 0.14 0.16 1.9e-01
Model I
55 mW/m²
Age: 12.000000 Myr
Melt Fraction
0.0e+00 0.02 0.04 0.06 0.08 0.1 0.12 0.14 1.7e-01
Model 3
65 mW/m²
Age: 12.900000 Myr
Melt Fraction
0.0e+00 0.04 0.06 0.08 0.1 0.12 0.14 0.16 2.0e-01
Model I7
75 mW/m²
Temperature
400
600
800
1000
1200
1300
Phase
Continental Crust
Sub-continental Mantle
Asthenospheric Mantle
Serpentinized Mantle
Sediments
Crustal detachments
Mantle detachments
Intruded Mantle

606

Figure 5. The end-state of each GeoFLAC model with an initial mantle potential temperature of 1300 ºC. Models 11, 2, and 15 have a full-spreading rate of 1 cm/yr and models 1, 3, and 17 have a full-spreading rate of 2 cm/yr. They are further arranged by surface heat flux, from 55 to 75 mW/m^2 in descending order. Isotherms for 400, 600, 800, 1000, 1200, and 1300 ºC are plotted as well as the melt fraction (scaled for each individual model to bring out details for low melt fractions).

4.2.1 1300 ºC mantle potential temperature cases

Model 11: MPT = 1300ºC, SHF = 55 mW/m^2, full spreading rate = 1 cm/yr. There's no clear rift axis, nor is there any melt production occurring. Incredibly large boudinage of the lithosphere with complex interactions between crustal and mantle detachment faults and shear zones (still anastomosing).

Model 2: MPT = 1300ºC, SHF = 65 mW/m^2, full spreading rate = 1 cm/yr. A very asymmetric rift where the right flank shows a large, complex network of anastomosing detachment faults in the subcontinental mantle beneath a thinned continental crust while the left flank shows tens of kilometers of denuded mantle and allochthonous crustal blocks near the seafloor spreading axis. Magma production is highly localized and only reaches 8.3% partial melt. The mechanical oceanic lithosphere is 16 km thick above the melt triangle, which is twice as thick as Model 1 where the thermal conditions are the same but extension rate is halved.

Model 15: MPT = 1300ºC, SHF = 75 mW/m^2, full spreading rate = 1 cm/yr. A very asymmetric and melt-poor rift. Widespread exhumation of the asthenospheric mantle serpentinization. There is a large block of continental lithosphere separated from the right rift flank by exhumed asthenospheric mantle. There is very little magmatic accretion and the melt producing region is irregularly shaped and deep. Melt fraction peaks at 2.5% and the mechanical oceanic lithosphere is 20 km thick.

Model 1: MPT = 1300ºC, SHF = 55 mW/m^2, full spreading rate = 2 cm/yr. A moderately asymmetric rift with large (>20 km long) boudins of subcontinental mantle, widely distributed crustal allochthons, and doming of the mantle beneath continental crust and at the continent-ocean transition. The highest degree of magma production is 19% partial melting localized beneath the estimated seafloor spreading axis (white, vertical bar). Anastomosing detachment faults (in red) extend the subcontinental mantle, especially where adjacent to mantle domes. The mechanical oceanic lithosphere is 10 km thick above the melt triangle.

Model 3: MPT = 1300ºC, SHF = 65 mWm^2, full spreading rate = 2 cm/yr^1. A slightly asymmetric rift with a wider left flank than right flank. Allochthons are widespread, with a large crustal block on the right flank. Anastomosing detachment faults are present in the mantle lithosphere, but only on the right flank and to a minor extent. At peak melt production, 20% partial melting is reached, and the region of melting is more distributed than in Model 2. The mechanical oceanic lithosphere is thinned to only 9 km at the seafloor spreading axis.

Model 17: MPT = 1300ºC, SHF = 75 mW/m^2, full spreading rate = 2 cm/yr. This case exhibits a wide, mostly symmetrical structure, limited anastomosing faults (until the onset of seafloor spreading), and limited lithospheric boudinage. Subcontinental mantle is not exhumed much, but widespread crust allochthons sit atop exhumed and intruded asthenospheric mantle. Relatively isotropic magmatic accretions on both rift flanks forms a mechanical oceanic lithosphere only 8 km thick. Melt fraction peaks at 20%.

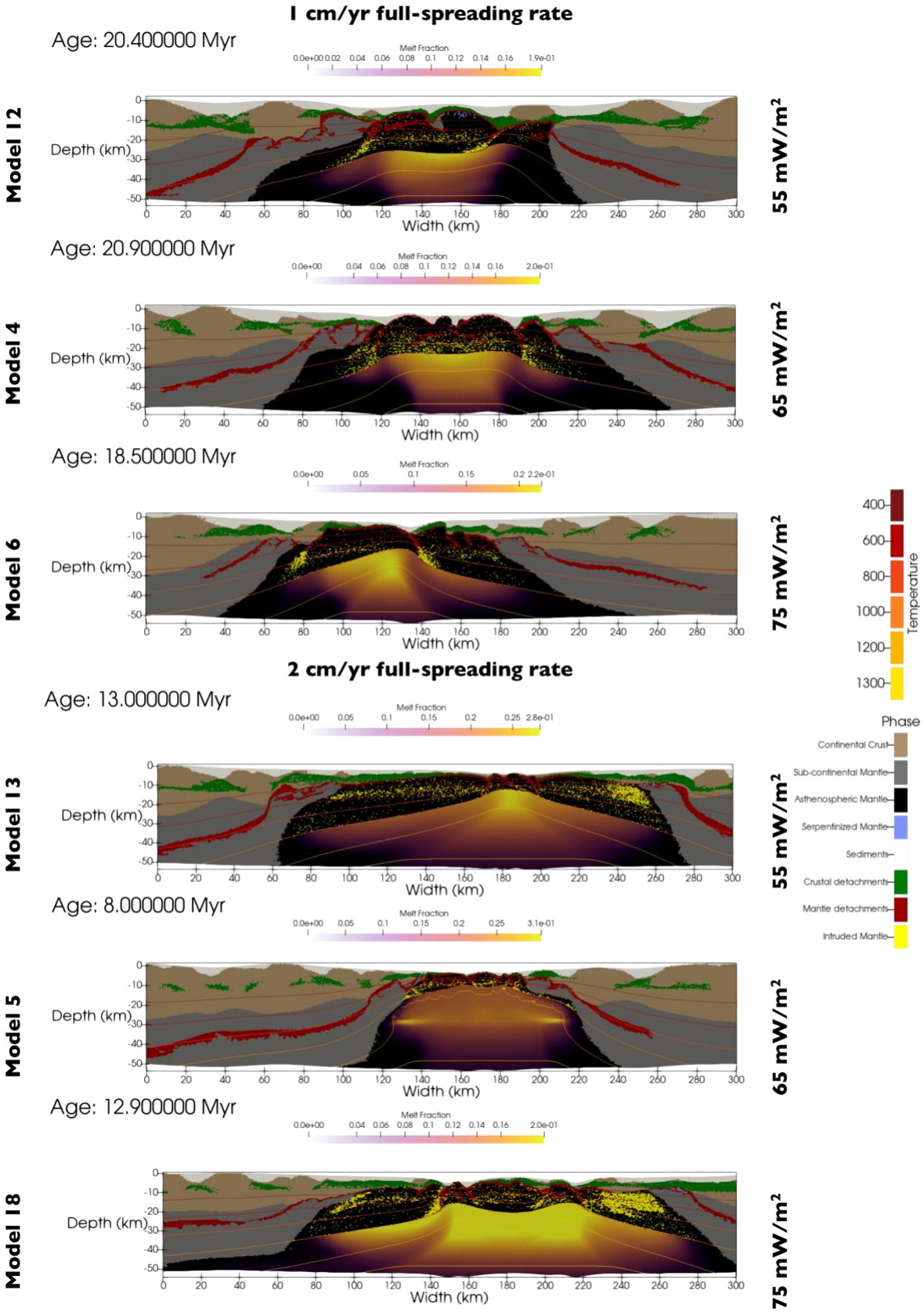
1 cm/yr full-spreading rate
Age: 20.400000 Myr
Model I2
55 mW/m²
Age: 20.900000 Myr
Model 4
65 mW/m²
Age: 18.500000 Myr
Model 6
75 mW/m²
2 cm/yr full-spreading rate
Age: 13.000000 Myr
Model I3
55 mW/m²
Age: 8.000000 Myr
Model 5
65 mW/m²
Age: 12.900000 Myr
Model I8
75 mW/m²
Melt Fraction
Depth (km)
Width (km)
Temperature
Phase
Continental Crust
Sub-continental Mantle
Asthenospheric Mantle
Serpentinized Mantle
Sediments
Crustal detachments
Mantle detachments
Intruded Mantle

650

Figure 6. The end-state of each GeoFLAC model with an initial mantle potential temperature of 1350 ºC. Models 12, 4, and 6 have a full-spreading rate of 1 cm/yr and models 13, 5, and 8 have a full-spreading rate of 2 cm/yr. They are further arranged by surface heat flux, from 55 to 75 mW/m^2 in descending order. Isotherms for 400, 600, 800, 1000, 1200, and 1300 ºC are plotted as well as the melt fraction (scaled for each individual model to bring out details for low melt fractions).

4.2.2 1350 ºC mantle potential temperature cases

Model 12: MPT = 1350ºC, SHF = 55 mW/m^2, full spreading rate = 1 cm/yr. Widespread denudation and anastomosing detachment faults, with both crustal and sub-continental mantle boudins present. The mechanical oceanic lithosphere is 18 km thick at the rift axis. The rift is very asymmetric. The left flank is wide and exhibits anastomosing faults, moderate magmatic accretion, and small allochthons of continental provenance. The right flank is narrow, with only slight accretion and a large block of continent crust derived from the H-block. Melt fraction reaches 19% at lithospheric rupture and break-up. Serpentinization is more widespread here than in any other case.

Model 4: MPT = 1350ºC, SHF = 65 mW/m^2, full spreading rate = 1 cm/yr. Another slightly asymmetric rift, but with a more complex structure than Model 3. There is major doming and exhumation of the mantle, with rolling hinge detachment faults extending both the sub-continental mantle and former asthenosphere. Anastomosing detachments are present in the right flank, but small scale (~2 km across). On the left flank, normal faults which merge into a roof detachment along the Moho deform a sub-continental mantle boudin. Peak melt production reached 20% partial melt. The mechanical oceanic lithosphere is very thick at 19 km. Asthenospheric buoyancy is also large since the active melt lithospheric layer is 20% filled with melt. This may explain the high domal topography observed near the rift axis and the large proportion of recrystallized melt pods in the mechanical oceanic lithosphere.

Model 6: MPT = 1350ºC, SHF = 75 mW/m^2, full spreading rate = 1 cm/yr. A moderately asymmetric rift with widespread. The left flank of the rift hosts a 20 km across crustal boudin and anastomosing mantle detachment faults, while the right flank hosts high-angle normal faults which exhumes the melt active mantle into the mechanical layer forming a large mantle core complex. Melt production peaks at 22% partial melt, and melt crystallization is especially concentrated in the shear zones beneath rolling hinge detachment faults. The mechanical oceanic lithosphere is relatively thick at 12 km at the seafloor spreading rift axis. Again, the spreading rates controls the thickness of the mechanical ocean lithosphere.

Model 13: MPT = 1350ºC, SHF = 55 mW/m^2, full spreading rate = 2 cm/yr. This case is a slightly asymmetric rift with widespread crustal allocthons. The melt fraction reaches 28% and melt crystallization is lopsided towards the right rift flank. The left flank has extensively anastomosed shear zones in the subcontinental mantle yet has relatively few mantle megamullions. The mechanical oceanic lithosphere is 8 km thick at the seafloor spreading axis.

Model 5: MPT = 1350ºC, SHF = 65 mW/m^2, full spreading rate = 2 $cm.yr^{-1}$. A slightly asymmetric rift based on the wider left flank than right flank. The rift also demonstrates minor doming of the mantle and anastomosing detachment faults on the left flank which are less prominent on the right flank. 31% partial melting is reached. The “bottom-heavy” distribution below the rift flanks indicates that the melt should extrude or intrude the lower continental crust

694 in a more realistic model with melt percolation. At the seafloor spreading axis, the mechanical
695 oceanic lithosphere is 6 km thick, which very thin and likely caused the high initial surface heat
696 flow, MPT and fast spreading rate.

697 **Model 18:** MPT = 1350ºC, SHF = 75 mW/m^2, full spreading rate = 2 cm/yr. Due to a lack of
698 melt extraction in this formulation of GeoFLAC, deformation has localized into two different rift
699 axes. Accounting for this, this case has a very similar structure as Models 17 and 19: widespread
700 crustal allochthons, lack of exhumed sub-continental mantle, and wide flanks; except that
701 magmatic accretion is elevated and concentrated on the right flank. The mechanical lithosphere
702 is 11 km thick and the melt fraction peaks at 25%.

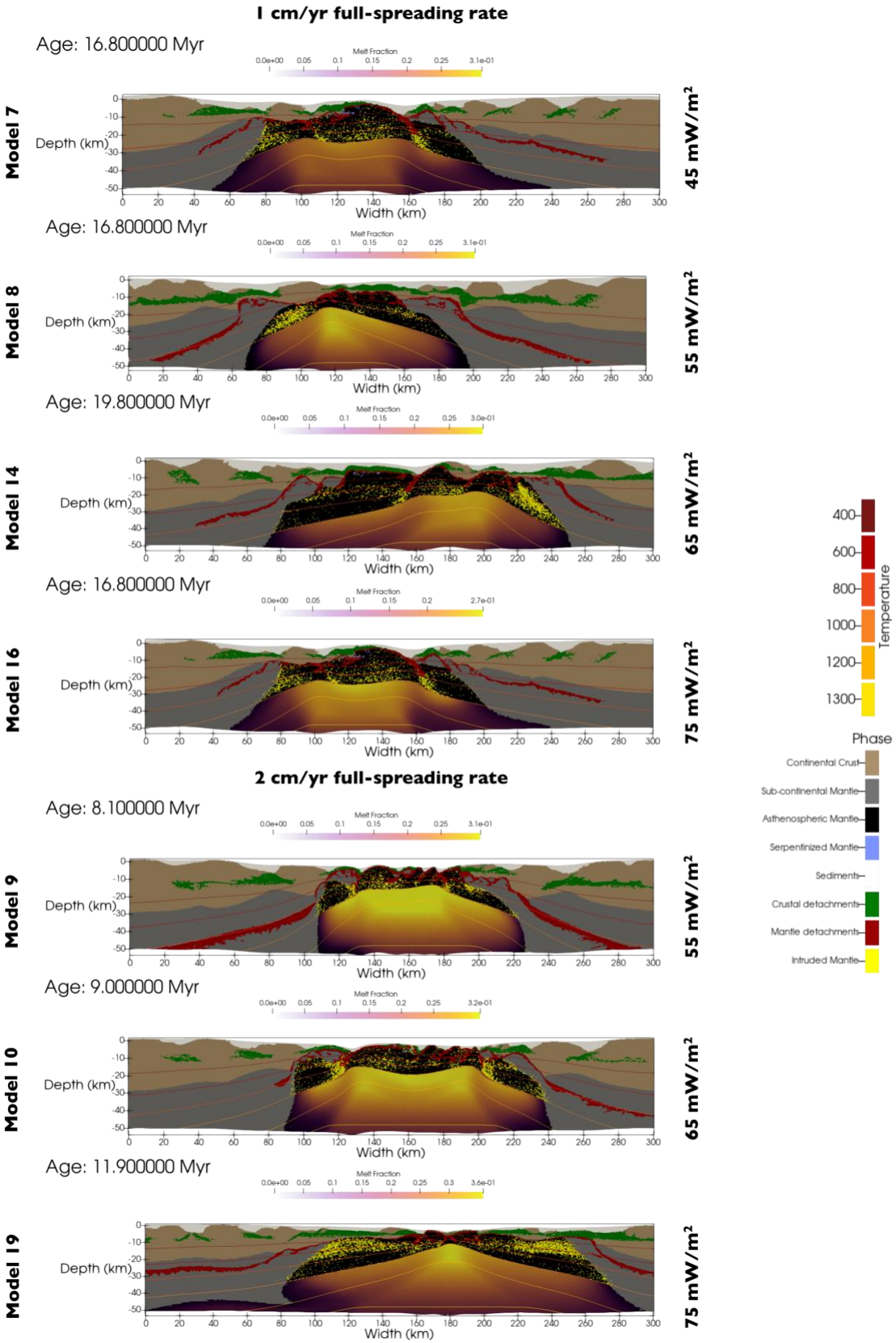
1 cm/yr full-spreading rate
Age: 16.800000 Myr
Model 7
45 mW/m²
Age: 16.800000 Myr
Model 8
55 mW/m²
Age: 19.800000 Myr
Model 14
65 mW/m²
Age: 16.800000 Myr
Model 16
75 mW/m²
2 cm/yr full-spreading rate
Age: 8.100000 Myr
Model 9
55 mW/m²
Age: 9.000000 Myr
Model 10
65 mW/m²
Age: 11.900000 Myr
Model 19
75 mW/m²
Melt Fraction
Depth (km)
Width (km)
Temperature
Phase
Continental Crust
Sub-continental Mantle
Asthenospheric Mantle
Serpentinized Mantle
Sediments
Crustal detachments
Mantle detachments
Intruded Mantle

Figure 7. The end-state of each GeoFLAC model with an initial mantle potential temperature of 1350 ºC. Models 7, 8, 14, and 16 have a full-spreading rate of 1 cm/yr and models 9, 10, and 19 have a full-spreading rate of 2 cm/yr. They are further arranged by surface heat flux, from 55 (45 in the case of model 7) to 75 mW/m^2 in descending order. Isotherms for 400, 600, 800, 1000, 1200, and 1300 ºC are plotted as well as the melt fraction (scaled for each individual model to bring out details for low melt fractions).

4.2.3 1400 ºC mantle potential temperature cases

Model 7: MPT = 1400ºC, SHF = 45 mW/m^2, full spreading rate = 1 cm/yr. A very asymmetric rift system with a very buoyant mantle lithosphere. On the left flank, anastomosing detachment faults are large and hyperextend the sub-continental mantle for ~50 km, while the crust forms into boudins of a similar scale. On the right, the distance over which the sub- continental mantle is hyperextended is shortened to only ~30 km, with a whole-lithosphere boudins at the continent-ocean transition. Melt crystallization is again especially focused in the shear zones beneath anti-listric detachment faults. Peak partial melting is at 32%. The mechanical oceanic lithosphere is 15 km thick at the seafloor-spreading axis.

Model 8: MPT = 1400ºC, SHF = 55 mW/m^2, full spreading rate = 1 cm/yr. Another very asymmetric rift, but both structurally and magmatically. Melt is widespread and production peaks at 35% partial melt and the crystallization of that melt is concentrated on the left flank. The left rift flank also hosts a ~40 km long crustal boudin. Crustal allochthons are widespread throughout but are thicker on the right rift flank. Anastomosing detachment faults present throughout the crust-mantle contact. The mechanical oceanic lithosphere is 14 km thick at the seafloor-spreading axis.

Model 14: MPT = 1400ºC, SHF = 65 mW/m^2, full spreading rate = 1 cm/yr. Widespread crustal allochthons across a moderately asymmetric rift. The left flank has a greater degree of asthenospheric mantle exhumation, serpentinization, and subcontinental mantle boudinage. The right flank exhibits more magmatic accretion and possesses a large crustal block derived from the H-block. The melt fraction peaks at 28% and the mechanical oceanic lithosphere is 16 km thick.

Model 16: MPT = 1400ºC, SHF = 75 mW/m^2, full spreading rate = 1 cm/yr. This is showing an asymmetric rift with extensive crustal allochthons on the left rift flank. There is less boudinage of the subcontinental mantle and of the crust, limited mostly to the right rift flank. Anastomosing detachment faults are present along the Moho on the left flank where magmatic accretion is active. Peak melt production reaches 27% melt fraction and the mechanical lithosphere is 17 km.

Model 9: MPT = 1400ºC, SHF = 55 mW/m^2, full spreading rate = 2 cm/yr. This rift exhibits moderate asymmetry, with the left flank being significantly wider than the right flank and hosting a sequence of sub-continental mantle boudins and mantle domes. Anastomosing detachment faults are prominent along the hyperextended mantle. Crystallization of melt is especially focused in the shear zones beneath detachment faults in the mantle. Partial melting is widespread and reaches 35% and the mechanical oceanic lithosphere is 10 km thick at the seafloor-spreading axis.

Model 10: MPT = 1400ºC, SHF = 65 mW/m^2, full spreading rate = 2 cm/yr. Structurally very similar to Model 9, but with wider margins and slightly less partial melting (32%). The mechanical oceanic lithosphere is 11 km thick, melt crystallization is focused in the shear zones

of mantle detachment faults. This case is asymmetric, though some of this comes from deformation being localized in two locations due to the absence of melt extraction during sea-floor spreading to create true oceanic crust.

Model 19: MPT = 1400ºC, SHF = 75 mW/m^2, full spreading rate = 2 cm/yr. The structure of this case is nearly identical to Model 17: wide margins, widespread crustal allochthons, etc.; but with an elevated melt fraction of 36% and a greater degree of melt accretion. The mechanical oceanic lithosphere is particularly thin here: only 6 km thick.

4.3 Generalized numerical model results

Each of the nineteen models presented in this paper follow similar evolutionary stages, though the timing and spatial relations may be different based on extension rate or thermal conditions. As in Model 1, each rift scenario includes: **1)** Symmetrical shear zones dipping a low angle (< 20) away from the rift axis in the sub-continental mantle. These shear zones facilitate the necking of the lithosphere, the upwelling of the asthenosphere, and the focusing of the melt region beneath the rift axis. **2)** Seaward dipping detachment faults in the continental crust and high temperature landward dipping detachments faults in the mantle originating between 800ºC and 1000ºC. **3)** An anastomosing network of crustal and mantle detachment faults that exhume both sub-continental mantle and asthenosphere. The denuded asthenosphere eventually forms a new layer in the mantle lithosphere that is intruded by pods of recrystallized melt and is bounded at its base by active melt. This layer mechanically becomes part of the oceanic lithosphere in which brittle and ductile mechanical processes occur. We name it the "mechanical oceanic lithosphere." **4)** High temperature landward dipping detachment faults initially sole under the continent and couple with crustal faults to form core complexes. **5)** The region of melt production is a diffuse triangle that is focused beneath the rift axis. Increased buoyancy in this region drives the asthenosphere towards the surface, this motion is accommodated by the mantle shear zones described previously. As the asthenosphere moves upward, cools and passes through the solidus due to conductive cooling, melt crystallizes above the melt producing region and then migrates as solidified bodies laterally with the tectonic blocks. The density of crystallized melt increases towards the rift axis. **6)** Below the melt production region, latent heat of fusion of the melt causes the 1300ºC isotherm to be depressed, marking what we refer to as the "thermal lithosphere" through the rest of this article. High temperature mantle shear zones are active in the upper layer forming a ultraslow spreading oceanic crust (Bickert et al., 2020).

The end-states of each model case have important structural and compositional homologies. One is asymmetry, though the degree of asymmetry is highly variable. The width of one rifted margin or flank (the distance between the start of seafloor spreading and the relatively unattenuated continental crust) is often different from its conjugate. In addition, asymmetry also exists in the structure of the rifted margin, often with regards to the presence and scale of lithospheric boudins (mantle, crust, or both) and in whether the crust or sub-continental mantle extends furthest towards the rift axis.

Another structural feature present throughout is the "shelf" of sub-continental mantle protruding below the thinned continental crust. It is visible where the lithosphere-scale mantle shear zones and detachment faults create a platform of mantle on each flank of the rift underlying the continental crust. These shelves form as the mantle is upwelled to 15-10 km depth and sub-horizontal anastomosing faults begin to accommodate hyperextension and exhumation. The shelf shallows towards the rift axis, but often forms domes or boudins of sub-continental mantle. It can

also have highly variable dimensions in different rift flanks and different model cases, ranging from ~5 km to >50 km across. The mantle detachment faults that form these boudins, domes, and mantle core-complexes generally dip landward in contrast to the earlier, continental detachments that dip seaward.

Melt crystallization (also referred to as underplating, magmatic accretion, or refertilization) in our models occurs above the melting region before being migrated laterally as rift evolves. Melt crystallization is also enhanced in high temperature mantle shear zones that form the soles of anti-listric detachment faults. Sometimes this leads to underplating being concentrated on one rift flank rather than another. This magmatic accretion forms the proto- oceanic and oceanic lithosphere.

By varying mantle potential temperature (MPT), surface heat flux (SHF), and extension rate it is possible to predict specific features in each rifted margin case. Structural trends are difficult to quantify, such as degree of asymmetry or the scale of extensional duplexes/ anastomosing faults. However, such structural trends are important predictions for future geological and geophysical observations. A summary of these observable properties in each model can be found in Supplementary Table 1.

The scale of anastomosing detachment faults (quantified by measuring the maximum and minimum widths of individual extensional duplexes within the mantle detachment fault system in each model) appears inversely correlated with surface heat flux. The less heat flowing through the lithosphere, the stronger it is and the larger the individual anastomosed, sigmoidal blocks within the detachment fault systems (Fig. S3). The relationship between SHF and extensional duplexes is also clear in the correlation between SHF and the number of individual anastomosed blocks, which decreases with increased SHF (Fig. S9). However, the frequency of anastomosed blocks has a slight, positive relationship with MPT (Fig. S8).

One of the most important and most obvious trends in the data is the correlation between mechanical oceanic lithosphere thickness and full spreading rate. Of the two extension rates tested using GeoFLAC, the 1 cm/yr cases consistently produce thicker oceanic lithosphere than their 2 cm/yr counterparts (Fig. S4). The thickness of the oceanic lithosphere doesn't have a clear correlation to either MPT or SHF (Figs. S5 & S6), though this may just be a limit of our models, which don't include the effects of melt extraction and volcanism on building oceanic crust. Relationships between MPT, SHF, and oceanic lithosphere thickness should be consistent with the observations of oceanic lithosphere at fast- and slow- spreading ridges (Langmuir & Forsyth, 2007; Macdonald, 2001; Searle, 2013), and thus melt extraction is an important caveat regarding this work. Mantle exhumation, quantified here by the number of mantle core complexes (domes of mantle material) that develop, is observed to decrease as SHF increases (Fig. S9). However, colder MPT cases exhibit larger core complexes that are not associated with the initiation of seafloor spreading (Fig. 5) Given that melt extraction has not been implemented, this result reflects a bias towards physical processes associated with amagmatic extension in our models.

The degree of partial melting and of melt crystallization is also observed to be a function of MPT and of extension. In the 1300ºC MPT cases, the percentage of partial melt ranges from 3% to 20%. For cases with a MPT of 1400ºC the percentage of partial melt ranges from 27% to 36%, a smaller range but with greater percentage melt (Fig. S5). A similar relationship holds for extension rate, where range of melt fractions is 3-35% for 1 cm/yr full spreading rates and 19-36% for 2 cm/yr full spreading rates (Fig. S4). The crystallization of this melt in the form of

underplating or magmatic accretion also increases with MPT and SHF, as seen from the general increase in crystallization from the top to bottom and from left to right of Fig. 4. The relatively high percentage of partial melt in some of these cases may be a result of our lacking of melt extraction; fractionation, melt conduits, and heterogeneities in the mantle among other necessary simplifications in our numerical models may change the parameters that determine melt percentage. However, the trends and structures observed in each model appear to reflect observed features of real rifted margins, especially the Ivorian margin.

5 Discussion

The experiments in GeoFLAC give new insight into the rifting processes. Our numerical modeling results provide a framework for the kinematic and magmatic development of rifted margins. Extension of the mantle lithosphere during the necking phase is accommodated by large, lithosphere-scale shear zones in the mantle that dip under the continental lithosphere and away from the rift axis. As per Ruh et al. (2022), these shear zones are regions where grain-size reduction enhances diffusion creep and weakens the lithosphere to the point where it can rupture. In previous work, models that don't incorporate dynamic grain recrystallization lack some key features shown in this article. Without dynamic grain recrystallization, there is no change in fault orientation during the emplacement of oceanic lithosphere, no doming of the mantle in core-complexes, and no lithospheric-scale mantle shear zones (e.g., Lavier et al., 2019). Since the Ivorian, Alpine Tethys, Uralide, and other margins (Clerc et al., 2018) show evidence of out-of-sequence detachment faults, mantle core complexes, and anastomosing shear zones it can be surmised that dynamic recrystallization plays a major role in continental rifting. Serpentinization, while present in some models, does not play an important role and is limited to the shallow crust at low temperature, where H_2O is available. Decompression melting in the mantle under the rift axis increases the buoyancy of the mantle and enhances upwelling of the asthenosphere along the lithosphere-scale mantle shear zones. This is a mechanism by which the mantle lithosphere is attenuated and asthenospheric material is brought towards the surface as part of lithospheric breakup.

The origin of the out-of-sequence (continentward-dipping), anastomosing detachment faults observed in the Ivorian continent-ocean transition, and in ophiolites like Nurali and Lanzo is also shown by our numerical modeling results. As the lithospheric shear zones shallow, they couple with crustal detachment faults and initiate the exhumation phase of rifting. The shear zones then transition into the anastomosing faults described previously (the distal or out-of-sequence detachment fault system). There is a weak inverse correlation between surface heat flux and the width of anastomosing faults (the size of each extensional duplex). A possible explanation for this is that the feedback loop between grain damage and dislocation creep which mechanically weakens the lithosphere is inhibited by a colder, stronger lithosphere (de Bresser et al., 2001; Tullis & Yund, 1985). The orientation of these out-of-sequence detachment faults is important. Under the stress regime imposed by buoyant, melt-rich mantle, they dip away from the rift axis and towards the continent. This interpretation is supported by the unusual strike of the out-of-sequence faults at the Ivorian margin. There, the out-of-sequence faults strike NNE while the rift axis trends NNW. If the anomalous orientation of these faults were a solely function of the seafloor spreading stress environment, they should be parallel to the rift axis. If they were a function of the dextral stress imposed by the neighboring Romanche and St. Paul transform faults, then their orientation should represent *en echelon* faults and strike WNW, nearly perpendicular to the actual orientation. We hypothesize that this orientation is a result of the

upward push of irregular magma bodies beneath the rift. This idea is consistent with the nearby presence of a mantle core-complex that could have concentrated decompression melting underneath it (before migrating eastward relative to the rift axis due to extension) as seen especially in models 1, 6, 9, and 10.

Thus, transition from continental rifting to seafloor spreading is strongly influenced by how tectonism and magmatism interact. In the Ivory Coast margin, the earliest evidence of melt is the volcaniclastic-to-pillow basalt that comprises Unit 6. Near the continent, this unit starts out thin, only a few tens of meters thick. However, as the rift develops and the rift axis migrates seaward relative to the continent, Unit 6 thickens to ~1 km and is characterized by more chaotic reflectors (pillow lavas). This increase in volcanism correlates to the shallowing and growth of the melting region of the asthenosphere as modeled by GeoFLAC. Dunite channels (Kelemen et al., 1995; Liang et al., 2010) and faults, such as documented in the Lanzo Massif (Müntener & Piccardo, 2003), provide conduits for this melt to erupt sub-aerially. The shallowing melt region also creates sheared gabbroic bodies that appear in the footwall of the anastomosing detachment faults as Unit 8 (gabbroic bodies also appear as isolated features in the sub-continental mantle of Unit 5). This is consistent with magmatic accretion seen in our GeoFLAC results. Magma that migrates past the solidus as it advects crystallizes above the melt triangle, accreting new crust or refertilizes ancient mantle lithosphere. Because the out-of-sequence detachment faults facilitate mantle upwelling, accretion is concentrated in footwalls of the detachment faults. The out-of-sequence system emplaces these gabbroic magma bodies, which source from (via faults or dunite channels as conduits) (Liang et al., 2010) sheeted dikes and pillow basalts of Unit 6. Thus, the network of detachment faults and the attenuation of the lithosphere above the decompression melting region control the onset of seafloor spreading and determine the structure of the continent-ocean transition.

New oceanic lithosphere in our GeoFLAC formulation comes in two flavors. The mechanical oceanic lithosphere forms above the melt triangle from upwelled asthenosphere and crystallized magma. In cases with a faster extension rate, the mechanical oceanic lithosphere is thinner as the high temperature asthenosphere is upwelling faster than it dissipates heat. Melt crystallization is focused under anti-listric shear zones and detachment faults because these are regions where the melt-rich asthenosphere passed through the solidus with greater frequency than elsewhere. The thermal oceanic lithosphere is defined by the 1300ºC isotherm, which sits beneath the melt triangle due to the latent heat of fusion depressing the geotherm at those depths. Because melt extraction is not part of our GeoFLAC formulation, oceanic *crust* is not included in our simulated oceanic lithosphere.

6 Conclusions

Synthesizing results from the Alpine Tethys margin and from the Ivorian margin with the GeoFLAC modeling provides a framework to understand rifted margin evolution at magma-poor margins. All three lines of evidence point towards homologous processes that control rifted margin evolution: high-temperature, anastomosing detachment faults that facilitate hyperextension; shear zones in the mantle lithosphere that facilitate the upwelling of asthenosphere driven by buoyancy; and increasing melt production as continents migrate away from the rift axis leading to magmatic accretion, seafloor spreading, and a change in the local stress environment (Fig. 8).

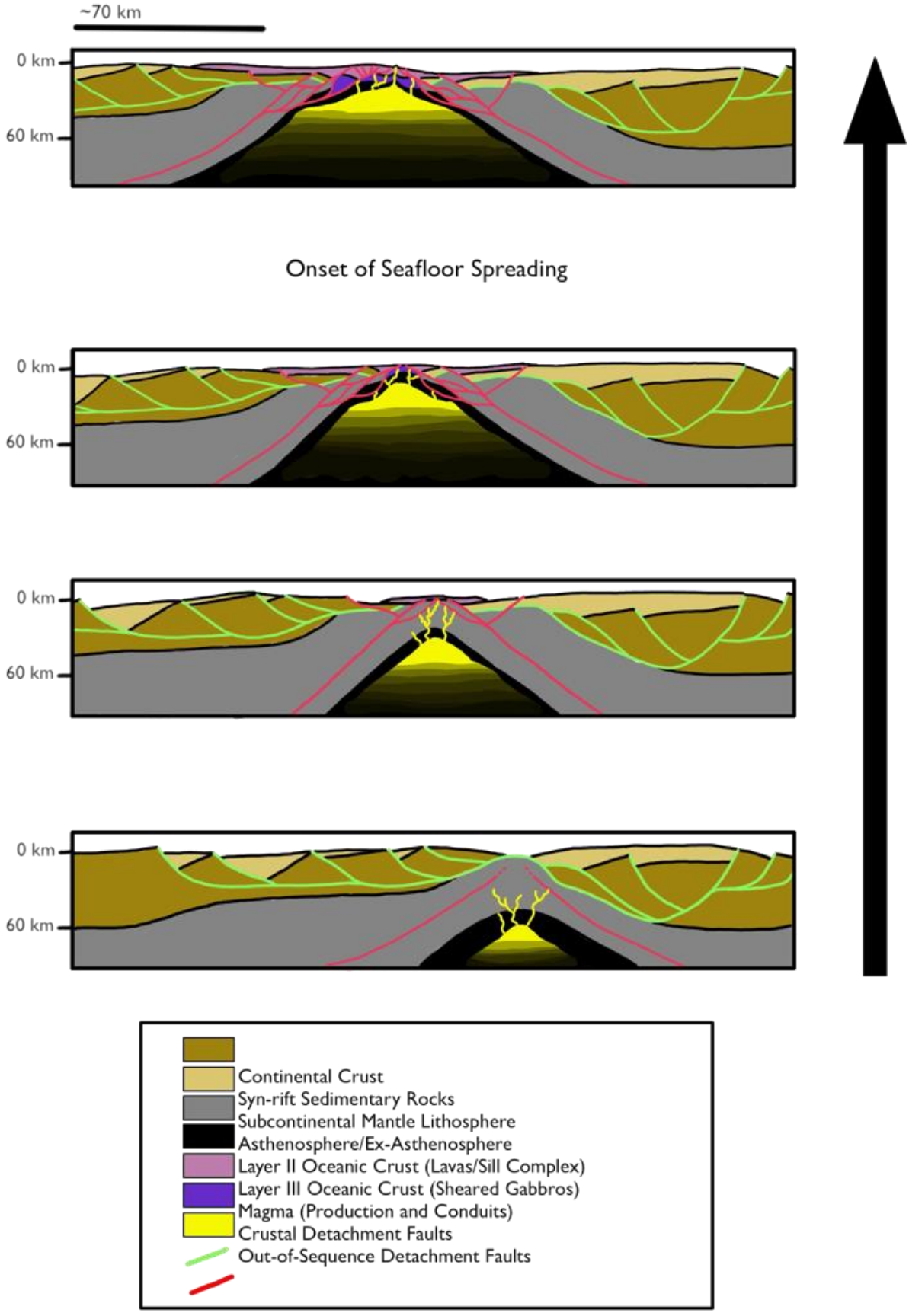
~70 km
0 km
60 km
Onset of Seafloor Spreading
0 km
60 km
0 km
60 km
0 km
60 km
Continental Crust
Syn-rift Sedimentary Rocks
Subcontinental Mantle Lithosphere
Asthenosphere/Ex-Asthenosphere
Layer II Oceanic Crust (Lavas/Sill Complex)
Layer III Oceanic Crust (Sheared Gabbros)
Magma (Production and Conduits)
Crustal Detachment Faults
Out-of-Sequence Detachment Faults

Figure 8. The conceptual, generalized model of the lava-poor rift-to-drift transition based on the numerical model results, paleomargin geology, and Deep Ivory Coast Basin seismic experiments. After the asymmetric, continental detachment fault system forms during the exhumation phase of rifting, symmetric, out-of-sequence detachment faults that are kinematically linked to lithospheric shear zones form in association with mantle core complexes. These new faults dip toward the continent and reflect a change in the stress environment due to the buoyant force of magma upwelling from below. As this new, mantle detachment fault system develops it splits into multiple, anastomosing faults to extensional duplexes of sub-continental mantle and formerly asthenospheric mantle. In the footwalls of these faults, mantle that has been intruded by mafic melts (magmatically accreted) is brought up to form the first Layer 3 of oceanic crust. Meanwhile, the volume of volcanism increases as the lithosphere at the rift axis thins and more conduits for melt (dikes, dunite channels, and detachment faults) form. These volcanic units (sheeted dike complexes, volcaniclastics, and lava flows) eventually form into Layer 2a and 2b of oceanic crust. Thus, the initiation of seafloor spreading is a transitional process between gravitational forced extensional tectonics and magmatically forced extensional tectonics.

In the early phases of the rift-to-drift transition, extension is expressed first through normal faults and then through detachment faults that dip towards the rift axis and cut through pre-rift sedimentary units and continental crust before soling into the subcontinental mantle. Lithospheric scale shear zones then develop in the mantle lithosphere which accommodate asthenospheric and subcontinental mantle upwelling (Fig. 8, bottom panel). These shear zones are the result of grain size reduction and DRX which enhance dislocation creep in olivine (Bickert et al., 2020; Ruh et al., 2022; Warren & Hirth, 2006). Decompression melting accelerates the upwelling of the asthenosphere until that the initial system of detachment faults couples with the mantle shear zones to exhume sub-continental mantle. As the melt region grows and shallows, it changes the stress regime of the rifting lithosphere and a system of anastomosing, out-of-sequence detachment faults with opposite dip-directions forms (Fig. 8, lower middle panel). The shallowness of this melt producing regions connects the melt triangle to shallow crustal depths via dikes, shear zones, and dunite channels (Kaczmarek & Müntener, 2008; Liang et al., 2010; Liu & Buck, 2021; Müntener & Piccardo, 2003). This leads to increasing volcanism and magmatism seaward, including the development of layered oceanic crust via sill and dike intrusions at the rift axis (which later becomes the footwall of the out-of-sequence detachment system). The new detachment fault system further exhumes the mantle, creating core-complex-like domes of peridotite that form the boundary between the hyperextended continental lithosphere from the newly created oceanic lithosphere (Fig. 8, upper middle & top panels).

This model for magma-poor rifted margin evolution shows the importance of melt production in determining the large-scale structures. Decompression melting accelerates the process of mantle upwelling, which in turn drives the exhumation phase of rifting and the transition in stress regime from gravity-driven (top-down, with faults dipping towards the rift axis) to melt-driven (bottom-up, with faults dipping away from the rift axis) during the rift-to-drift transition. Additionally, the anastomosing high temperature shear zones may provide conduits for melt to pool, to source a dike and sill network, or to follow fracture networks which initiate volcanism and then seafloor spreading as the volume of melt increases.

This framework for understanding magma-poor rifts allows us to put different rifted margins into context (Fig. 9). Comparing the Ivorian margin, the Err-Platta Nappes, and the Lanzo Massif to

the conceptual model (from Fig. 8, top panel) show how building blocks or rifted margins exposed at Earth surface are homologous to sections of the simulated rifted margins. Err-Platta (outlined in magenta) is a homology of the shallower region of hyperextension, where the mantle domes upwards in contact with syn-rift sedimentary rocks (Manatschal et al., 2007). Down section and deeper, Lanzo (outlined in orange) is homologous with the region where formerly asthenospheric mantle is brought up against sub-continental mantle by anastomosing faults to form an extensional duplex. This region is also where melt intrusion has created proto-oceanic lithosphere (Kaczmarek & Müntener, 2008). The homologous equivalent of the Ivorian margin (outlined in blue) overlaps both regions, but also extends to the first appearance of oceanic crust.

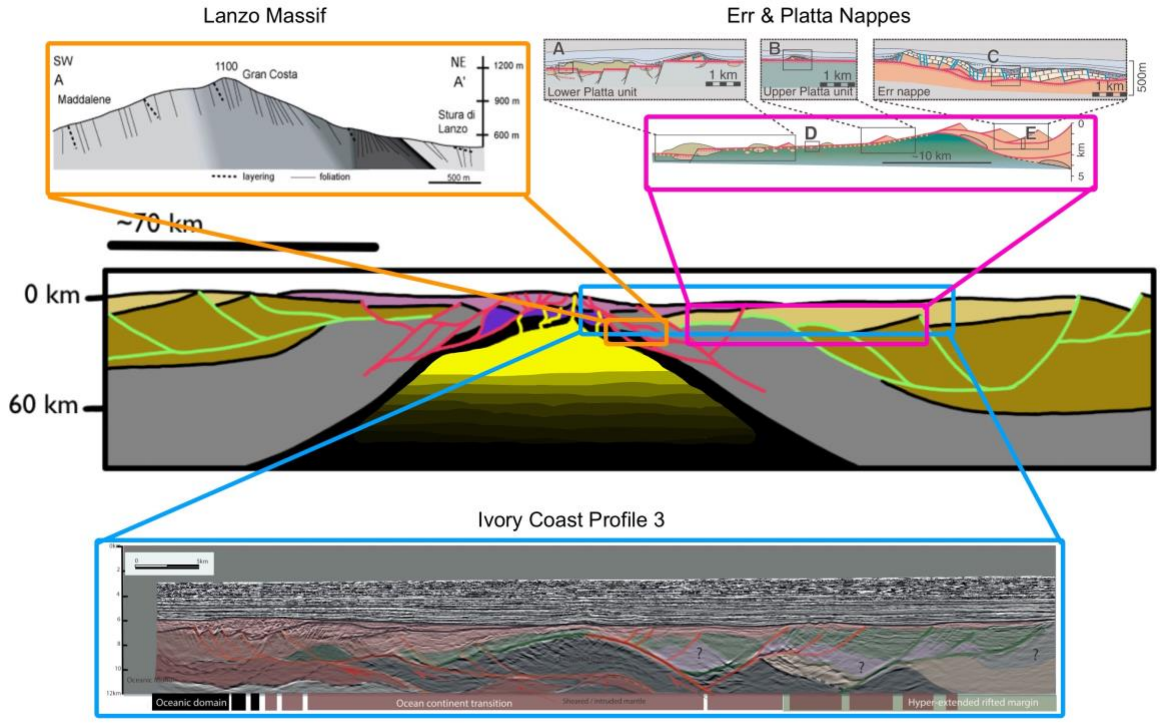

Figure 9. The conceptual model of lava-poor rifting in relation to the geological and geophysical evidence in the Alpine-Tethys paleomargin and the Ivory Coast rifted margin. The Err-Platta Nappes represent the up-section region of mantle doming and fault contacts with syn-rift sedimentary units. The Lanzo Massif represents a deeper, down-section region where the mantle is deforming in extensional duplexes and experiencing refertilzation. The Deep Ivory Coast section encompasses the entire rifted margin from extended continental crust to oceanic lithosphere. The cross sections for the Err & Platta Nappes were modified from Manatschal et al., (2007).

While we have applied this scheme to magma-poor rifted margin evolution, it potentially applies to other types of rifted margin or other tectonic boundaries. Under increased mantle potential temperatures, magmatism may occur earlier and to a greater extent. The SDRs and fault geometry seen in volcanic rifted margins could result from earlier magmatism changing the principal stress direction from top-down to bottom-up during the stretching phase and before widespread exhumation can begin. Future work synthesizing GeoFLAC results with geological and geophysical observations will test this hypothesis for volcanic margins such as along

994 Scandinavia, West India, and Argentina and their conjugates. If successful, this methodology
995 may be applied to pre-Mesozoic rift systems to investigate the effects of early-Earth thermal
996 conditions

997 **Acknowledgments**

998 Nicholas Montiel and Luc Lavier thank Petrobras SA for supporting our work through a
999 generous grant. We thank TotalEnergies SE for allowing publication of this work. We thank
1000 TGS ASA for permission to publish the geoseismic profiles interpreted from the TGS ASA
1001 seismic data from Ivory Coast. We'd also like to thank Suzon Jammes for providing comments
1002 on the manuscript.

1003 **Open Research**

1004 The seismic data are property of TGS ASA and can be accessed only with authorization of TGS
1005 ASA. The results of the numerical models in the form of .vtk files and .avi files for this study are
1006 available on Zenodo (https://zenodo.org at DOI: 10.5281/zenodo.7551549). The numerical code
1007 used for this study is available on GitHub at https://github.com/tan2/geoflac.

1008 **References**

1009 Allen, P. A., & Allen, J. R. (2013). *Basin Analysis: Principles and Application to Petroleum Play*
1010 *Assessment* (3rd Edition). Wiley-Blackwell. https://www.wiley.com/en-us/
1011 Basin+Analysis%3A+Principles+and+Application+to+Petroleum+Play+Assessment%2C+3rd+E
1012 dition-p-9780470673775

1013 Austin, N. J., & Evans, B. (2007). Paleowattmeters: A scaling relation for dynamically
1014 recrystallized grain size. *Geology*, *35*(4), 343–346. https://doi.org/10.1130/G23244A.1

1015 Basile, C., Mascle, J., Popoff, M., Bouillin, J. P., & Mascle, G. (1993). The Ivory Coast-Ghana
1016 transform margin: A marginal ridge structure deduced from seismic data. *Tectonophysics*, *222*(1),
1017 1–19. https://doi.org/10.1016/0040-1951(93)90186-N

1018 Basile, C., Mascle, J., & Guiraud, R. (2005). Phanerozoic geological evolution of the Equatorial
1019 Atlantic domain. *Journal of African Earth Sciences*, *43*(1-3), 275-282.

1020 Biari, Y., Klingelhoefer, F., Franke, D., Funck, T., Loncke, L., Sibuet, J.-C., Basile, C., Austin, J. A.,
1021 Rigoti, C. A., Sahabi, M., Benabdellouahed, M., & Roest, W. R. (2021). Structure and evolution
1022 of the Atlantic passive margins: a review of existing rifting models from wide-angle seismic data
1023 and kinematic reconstruction. *Marine and Petroleum Geology*, *126*(January), 104898.
1024 https://doi.org/10.1016/j.marpetgeo.2021.104898

1025 Bickert, M., Cannat, M., Tommasi, A., Jammes, S., & Lavier, L. (2021). Strain Localization in the
1026 Root of Detachment Faults at a Melt-Starved Mid-Ocean Ridge: A Microstructural Study of
1027 Abyssal Peridotites From the Southwest Indian Ridge. *Geochemistry, Geophysics, Geosystems*,
1028 *22*(5). https://doi.org/10.1029/2020GC009434

1029 Bickert, M., Lavier, L., & Cannat, M. (2020). How do detachment faults form at ultraslow mid-
1030 ocean ridges in a thick axial lithosphere? *Earth and Planetary Science Letters*, *533*, 116048.
1031 https://doi.org/10.1016/j.epsl.2019.116048

1032 Blackman, D. K., Ildefonse, B., John, B. E., Ohara, Y., Miller, D. J., Abe, N., Abratis, M., Andal,
1033 E. S., Andreani, M., Awaji, S., Beard, J. S., Brunelli, D., Charney, A. B., Christie, D. M., Collins,
1034 J., Delacour, A. G., Delius, H., Drouin, M., Einaudi, F., … Zhao, X. (2011). Drilling constraints

on lithospheric accretion and evolution at Atlantis Massif, Mid-Atlantic Ridge 30N. *Journal of Geophysical Research: Solid Earth*, *116*(7), 1–25. https://doi.org/10.1029/2010JB007931

Boillot, G., Recq, M., Winterer, E. L., Meyer, A. W., Applegate, J., Baltuck, M., Bergen, J. A., Comas, M. C., Davies, T. A., Dunham, K., Evans, C. A., Girardeau, J., Goldberg, G., Haggerty, J., Jansa, L. F., Johnson, J. A., Kasahara, J., Loreau, J. P., Luna-Sierra, E., … Williamson, M. (1987). Tectonic denudation of the upper mantle along passive margins: a model based on drilling results (ODP leg 103, western Galicia margin, Spain). *Tectonophysics*, *132*(4), 335–342. https://doi.org/10.1016/0040-1951(87)90352-0

Bronner, A., Sauter, D., Manatschal, G., Péron-Pinvidic, G., & Munschy, M. (2011). Magmatic breakup as an explanation for magnetic anomalies at magma-poor rifted margins. *Nature Geoscience*, *4*(8), 549–553. https://doi.org/10.1038/ngeo1201

Buck, W. R. (2006). The role of magma in the development of the Afro-Arabian Rift System. *Geological Society Special Publication*, *259*, 43–54. https://doi.org/10.1144/GSL.SP.2006.259.01.05

Cann, J. R. (1970). New Model for the Structure of the Ocean Crust. *Nature 1970 226:5249*, *226*(5249), 928–930. https://doi.org/10.1038/226928a0

Cann, J. R., Blackman, D. K., Smith, D. K., McAllister, E., Janssen, B., Mello, S., Avgerinos, E., Pascoe, A. R., & Escartin, J. (1997). Corrugated slip surfaces formed at ridge–transform intersections on the Mid-Atlantic Ridge. *Nature*, *385*(6614), 329–332. https://doi.org/10.1038/385329a0

Cho, H. E., Hammi, Y., Bowman, A. L., Karato, S., Baumgardner, J. R., & Horstemeyer, M. F. (2019). A unified static and dynamic recrystallization Internal State Variable (ISV) constitutive model coupled with grain size evolution for metals and mineral aggregates. *International Journal of Plasticity*, *112*, 123–157. https://doi.org/10.1016/j.ijplas.2018.08.009

Clerc, C., Ringenbach, J. C., Jolivet, L., & Ballard, J. F. (2018). Rifted margins: Ductile deformation, boudinage, continentward-dipping normal faults and the role of the weak lower crust. *Gondwana Research, 53*, 20–40. https://doi.org/10.1016/J.GR.2017.04.030

Davis, G. H. (1983). Shear-zone model for the origin of metamorphic core complexes. *Geology*, *11*(6), 342. https://doi.org/10.1130/0091-7613(1983)11<342:SMFTOO>2.0.CO;2

Davis, J. K., & Lavier, L. L. (2017). Influences on the development of volcanic and magma-poor morphologies during passive continental rifting. *Geosphere*, *13*(5), 1524–1540. https://doi.org/10.1130/GES01538.1

Davis, M., & Kusznir, N. (2016). 4. Depth-Dependent Lithospheric Stretching at Rifted Continental Margins. *Rheology and Deformation of the Lithosphere at Continental Margins*, 92–137. https://doi.org/10.7312/karn12738-005

de Bresser, J., ter Heege, J., & Spiers, C. (2001). Grain size reduction by dynamic recrystallization: can it result in major rheological weakening? *International Journal of Earth Sciences*, *90*(1), 28–45. https://doi.org/10.1007/s005310000149

Detournay, Christine., & Hart, R. D. (Roger D. (1999). *FLAC and numerical modeling in geomechanics : proceedings of the International FLAC Symposium on Numerical Modeling in Geomechanics, Minneapolis, Minnesota, USA, 1-3 September 1999*. Balkema.

Dilek, Y. (2003). Ophiolite concept and its evolution. In *Ophiolite concept and the evolution of geological thought*. Geological Society of America. https://doi.org/10.1130/0-8137-2373-6.1

Escartín, J., Hirth, G., & Evans, B. (2001). Strength of slightly serpentinized peridotites: Implications for the tectonics of oceanic lithosphere. *Geology*, *29*(11), 1023. https://doi.org/10.1130/0091-7613(2001)029<1023:SOSSPI>2.0.CO;2

Franke, D. (2013). Rifting, lithosphere breakup and volcanism: Comparison of magma-poor and volcanic rifted margins. *Marine and Petroleum Geology*, *43*, 63–87. https://doi.org/10.1016/J.MARPETGEO.2012.11.003

Fricke, H. C., Wickham, S. M., & O'neil, J. R. (1992). Contributions to Mineralogy and Petrology Oxygen and hydrogen isotope evidence for meteoric water infiltration during mylonitization and uplift in the Ruby Mountains-East Humboldt Range core complex, Nevada. In *Contrib Mineral Petrol* (Vol. 111).

Geoffroy, L., Burov, E. B., & Werner, P. (2015). Volcanic passive margins: Another way to break up continents. *Scientific Reports*, *5*. https://doi.org/10.1038/srep14828

Gillard, M., Autin, J., Karpoff, A.-M., Manatschal, G., Munschy, M., Sauter, D., & Schaming, M. (2013). Unravelling the process of continental breakup: a case study of the Australia-Antarctica conjugate margins. In *Geophysical Research Abstracts* (Vol. 15).

Gillard, M., Tugend, J., Müntener, O., Manatschal, G., Karner, G. D., Autin, J., Sauter, D., Figueredo, P. H., & Ulrich, M. (2019). The role of serpentinization and magmatism in the formation of decoupling interfaces at magma-poor rifted margins. *Earth-Science Reviews*, *196*, 102882. https://doi.org/10.1016/j.earscirev.2019.102882

Gómez-Romeu, J., Kusznir, N., Ducoux, M., Jammes, S., Ball, P., Calassou, S., & Masini, E. (2022). Formation of SDRs-Ocean transition at magma-rich rifted margins: Significance of a mantle seismic reflector at the western Demerara margin. *Tectonophysics*, *845*, 229624.

Hansen, L. N., Zimmerman, M. E., Dillman, A. M., & Kohlstedt, D. L. (2012). Strain localization in olivine aggregates at high temperature: A laboratory comparison of constant- strain-rate and constant-stress boundary conditions. *Earth and Planetary Science Letters*, *333– 334*, 134–145. https://doi.org/10.1016/J.EPSL.2012.04.016

Harding, J. L., Van Avendonk, H. J. A., Hayman, N. W., Grevemeyer, I., Peirce, C., & Dannowski, A. (2017). Magmatic-tectonic conditions for hydrothermal venting on an ultraslow- spread oceanic core complex. *Geology*, *45*(9), 839–842. https://doi.org/10.1130/G39045.1

Harkin, C., Kusznir, N., Tugend, J., Manatschal, G., & McDermott, K. (2019). Evaluating magmatic additions at a magma-poor rifted margin: An East Indian case study. *Geophysical Journal International*, *217*(1), 25–40. https://doi.org/10.1093/gji/ggz007

Hayman, N. W., Grindlay, N. R., Perfit, M. R., Mann, P., Leroy, S., & de Lépinay, B. M. (2011). Oceanic core complex development at the ultraslow spreading Mid-Cayman Spreading Center. *Geochemistry, Geophysics, Geosystems*, *12*(3), n/a-n/a. https://doi.org/10.1029/2010GC003240

Hess, H. H. (1962). History of Ocean Basins. *Petrologic Studies*, 599–620. https://doi.org/10.1130/PETROLOGIC.1962.599

Hirschmann, M. M., Tenner, T., Aubaud, C., & Withers, A. C. (2009). Dehydration melting of nominally anhydrous mantle: The primacy of partitioning. *Physics of the Earth and Planetary Interiors*, *176*(1–2), 54–68. https://doi.org/10.1016/j.pepi.2009.04.001

Hirth, G., & Kohlstedt, D. (2003). Rheology of the upper mantle and the mantle wedge: A view from the experimentalists. In *Geophysical Monograph Series* (Vol. 138, pp. 83–105). https://doi.org/10.1029/138GM06

Huismans, R., & Beaumont, C. (2011). Depth-dependent extension, two-stage breakup and cratonic underplating at rifted margins. *Nature*, *473*(7345), 74–78. https://doi.org/10.1038/ nature09988

Huismans, R. S., & Beaumont, C. (2008). Complex rifted continental margins explained by dynamical models of depth-dependent lithospheric extension. *Geology*, *36*(2), 163–166. https://doi.org/10.1130/G24231A.1

Huismans, R. S., & Beaumont, C. (2014). Rifted continental margins: The case for depth-dependent extension. *Earth and Planetary Science Letters*, *407*, 148–162. https://doi.org/10.1016/j.epsl.2014.09.032

Jonas, J. J., & Poliak, E. I. (2003). The Critical Strain for Dynamic Recrystallization in Rolling Mills. *Materials Science Forum*, *426–432*(1), 57–66. https://doi.org/10.4028/WWW.SCIENTIFIC.NET/MSF.426-432.57

Kaczmarek, M. A., & Müntener, O. (2008). Juxtaposition of melt impregnation and high-temperature shear zones in the upper mantle; field and petrological constraints from the lanzo peridotite (Northern Italy). *Journal of Petrology*, *49*(12), 2187–2220. https://doi.org/10.1093/PETROLOGY/EGN065

Kaczmarek, M.-A., & Müntener, O. (2005). Exhumation of mantle lithosphere: Field relations, and interaction processes between magmatism and deformation (field trip to the northern Lanzo peridotite). *Ofioliti*, *30*(2), 125–134. https://doi.org/10.4454/ofioliti.v30i2.246

Kaczmarek, M.-A., & Müntener, O. (2010). The variability of peridotite composition across a mantle shear zone (Lanzo massif, Italy): interplay of melt focusing and deformation. *Contributions to Mineralogy and Petrology, 160*(5), 663–679. https://doi.org/10.1007/s00410-010-0500-8

Katz, R. F., Spiegelman, M., & Langmuir, C. H. (2003). A new parameterization of hydrous mantle melting. *Geochemistry, Geophysics, Geosystems*, *4*(9), n/a-n/a. https://doi.org/10.1029/2002GC000433

Kelemen, P. B., Shimizu, N., & Salters, V. (1995). Extraction of mid-ocean-ridge basalt from the upwelling mantle.pdf. *Nature*, *375*, 747–753.

KUSZNIR, N. J., HUNSDALE, R., & ROBERTS, A. M. (2005). Timing and magnitude of depth-dependent lithosphere stretching on the southern Lofoten and northern Vøring continental margins offshore mid-Norway: implications for subsidence and hydrocarbon maturation at volcanic rifted margins. *Geological Society, London, Petroleum Geology Conference Series*, *6*(1), 767–783. https://doi.org/10.1144/0060767

Kusznir, N. J., & Karner, G. D. (2007). Continental lithospheric thinning and breakup in response to upwelling divergent mantle flow: application to the Woodlark, Newfoundland and Iberia

margins. *Geological Society, London, Special Publications*, *282*(1), 389–419. https://doi.org/10.1144/sp282.16

Labails, C., Olivet, J. L., Aslanian, D., & Roest, W. R. (2010). An alternative early opening scenario for the Central Atlantic Ocean. *Earth and Planetary Science Letters*, *297*(3-4), 355-368.

Langmuir, C., & Forsyth, D. W. (2007). Mantle Melting Beneath Mid-Ocean Ridges. *Oceanography*. https://dash.harvard.edu/handle/1/3685824

Lavier, L. L., Ball, P. J., Manatschal, G., Heumann, M. J., MacDonald, J., Matt, V. J., & Schneider, C. (2019). Controls on the Thermomechanical Evolution of Hyperextended Lithosphere at Magma-Poor Rifted Margins: The Example of Espirito Santo and the Kwanza Basins. *Geochemistry, Geophysics, Geosystems*, *20*(11), 5148–5176. https://doi.org/10.1029/2019GC008580

Lavier, L. L., Buck, W. R., & Poliakov, A. N. B. (2000). Factors controlling normal fault offset in an ideal brittle layer. *Journal of Geophysical Research: Solid Earth*, *105*(B10), 23431–23442. https://doi.org/10.1029/2000jb900108

Lavier, L. L., & Manatschal, G. (2006). A mechanism to thin the continental lithosphere at magma-poor margins. *Nature*, *440*(7082), 324–328. https://doi.org/10.1038/nature04608

Liang, Y., Schiemenz, A., Hesse, M. A., Parmentier, E. M., & Hesthaven, J. S. (2010). High-porosity channels for melt migration in the mantle: Top is the dunite and bottom is the harzburgite and lherzolite. *Geophysical Research Letters*, *37*(15), n/a-n/a. https://doi.org/10.1029/2010GL044162

Lindenfeld, M., & Rümpker, G. (2011). Detection of mantle earthquakes beneath the East African Rift. *Geophys. J. Int*, *186*, 1–5. https://doi.org/10.1111/j.1365-246X.2011.05048.x

Liu, Z., & Buck, W. R. (2021). Magmatic sill formation during dike opening. *Geology*, *50*(4), 407–411. https://doi.org/10.1130/G49400.1

Macdonald, K. C. (2001). Mid-ocean Ridge Tectonics, Volcanism And Geomorphology. In *Encyclopedia of Ocean Sciences* (pp. 1798–1813). Elsevier. https://doi.org/10.1006/rwos.2001.0094

Manatschal, G. (2004). New models for evolution of magma-poor rifted margins based on a review of data and concepts from West Iberia and the Alps. *International Journal of Earth Sciences*, *93*(3), 432–466. https://doi.org/10.1007/s00531-004-0394-7

Manatschal, G., Müntener, O., Lavier, L. L., Minshull, T. A., & Péron-Pinvidic, G. (2007). Observations from the Alpine Tethys and Iberia–Newfoundland margins pertinent to the interpretation of continental breakup. *Geological Society, London, Special Publications*, *282*(1), 291–324. https://doi.org/10.1144/SP282.14

Manatschal, G., & Nievergelt, P. (1997). A continent-ocean transition recorded in the Err and Platta nappes (Eastern Switzerland). *Eclogae Geologicae Helvetiae*, *90*(1), 3–27.

Manatschal, G., Sauter, D., Karpoff, A. M., Masini, E., Mohn, G., & Lagabrielle, Y. (2011). The Chenaillet Ophiolite in the French/Italian Alps: An ancient analogue for an Oceanic Core Complex? *Lithos*, *124*(3–4), 169–184. https://doi.org/10.1016/J.LITHOS.2010.10.017

Mascle, J., & Blarez, E. (1987). Evidence for transform margin evolution from the Ivory Coast–Ghana continental margin. *Nature*, *326*(6111), 378–381. https://doi.org/10.1038/326378a0

McCarthy, A., Falloon, T. J., Sauermilch, I., Whittaker, J. M., Niida, K., & Green, D. H. (2020). Revisiting the Australian-Antarctic Ocean-Continent Transition Zone Using Petrological and Geophysical Characterization of Exhumed Subcontinental Mantle. *Geochemistry, Geophysics, Geosystems*, *21*(7). https://doi.org/10.1029/2020GC009040

McIntosh, K., van Avendonk, H., Lavier, L., Lester, W. R., Eakin, D., Wu, F., Liu, C. S., & Lee, C. S. (2013). Inversion of a hyper-extended rifted margin in the Southern Central Range of Taiwan. *Geology*, *41*(8), 871–874. https://doi.org/10.1130/G34402.1

Moulin, M., Aslanian, D., & Unternehr, P. (2010). A new starting point for the South and Equatorial Atlantic Ocean. *Earth-Science Reviews*, *98*(1-2), 1-37.

Müntener, O., & Piccardo, G. B. (2003). Melt migration in ophiolitic peridotites: the message from Alpine-Apennine peridotites and implications for embryonic ocean basins. *Geological Society, London, Special Publications*, *218*(1), 69–89. https://doi.org/10.1144/ GSL.SP.2003.218.01.05

Nicolas, A. (1989). *Generation of Oceanic Crust* (pp. 253–285). Springer, Dordrecht. https://doi.org/10.1007/978-94-009-2374-4_11

Nirrengarten, M., Manatschal, G., Tugend, J., Kusznir, N. J., & Sauter, D. (2017). Nature and origin of the J-magnetic anomaly offshore Iberia–Newfoundland: implications for plate reconstructions. *Terra Nova*, *29*(1), 20–28. https://doi.org/10.1111/ter.12240

Nirrengarten, M., Manatschal, G., Tugend, J., Kusznir, N., & Sauter, D. (2018). Kinematic Evolution of the Southern North Atlantic: Implications for the Formation of Hyperextended Rift Systems. *Tectonics*, *37*(1), 89–118. https://doi.org/10.1002/2017TC004495

Pedrera, A., García-Senz, J., Ayala, C., Ruiz-Constán, A., Rodríguez-Fernández, L. R., Robador, A., & González Menéndez, L. (2017). Reconstruction of the Exhumed Mantle Across the North Iberian Margin by Crustal-Scale 3-D Gravity Inversion and Geological Cross Section. *Tectonics*, *36*(12), 3155–3177. https://doi.org/10.1002/2017TC004716

Pérez-Gussinyé, M., & Reston, T. J. (2001). Rheological evolution during extension at nonvolcanic rifted margins: Onset of serpentinization and development of detachments leading to continental breakup. *Journal of Geophysical Research: Solid Earth*, *106*(B3), 3961–3975. https://doi.org/10.1029/2000JB900325

Peron-Pinvidic, G., Manatschal, G., & Osmundsen, P. T. (2013). Structural comparison of archetypal Atlantic rifted margins: A review of observations and concepts. In *Marine and Petroleum Geology* (Vol. 43, pp. 21–47). Elsevier. https://doi.org/10.1016/ j.marpetgeo.2013.02.002

Piccardo, G. B., Zanetti, A., & Müntener, O. (2007). Melt/peridotite interaction in the Southern Lanzo peridotite: Field, textural and geochemical evidence. *Lithos*, *94*(1–4), 181–209. https:// doi.org/10.1016/j.lithos.2006.07.002

Platt, J. P., Behr, W. M., & Cooper, F. J. (2015). Metamorphic core complexes: windows into the mechanics and rheology of the crust. *Journal of the Geological Society*, *172*(1), 9–27. https://doi.org/10.1144/jgs2014-036

Poliak, E. I., & Jonas, J. J. (1996). A one-parameter approach to determining the critical conditions for the initiation of dynamic recrystallization. *Acta Materialia*, *44*(1), 127–136. https://doi.org/10.1016/1359-6454(95)00146-7

Poliakov, A. N. B., Cundall, P. A., Podladchikov, Y. Y., & Lyakhovsky, V. A. (1993). An explicit inertial method for the simulation of viscoelastic flow: an evaluation of elastic effects on diapiric flow in two- and three- layers models. *Flow and Creep in the Solar System: Observations, Modeling and Theory*, *1991*, 175–195. https://doi.org/10.1007/978-94-015-8206-3_12

Puchkov, V. N. (2009). The evolution of the Uralian orogen. *Geological Society, London, Special Publications*, *327*(1), 161–195. https://doi.org/10.1144/SP327.9

Reston, T. (2018). Flipping detachments: The kinematics of ultraslow spreading ridges. *Earth and Planetary Science Letters*, *503*, 144–157. https://doi.org/10.1016/j.epsl.2018.09.032

Ros, E., Pérez-Gussinyé, M., Araújo, M., Thoaldo Romeiro, M., Andrés-Martínez, M., & Morgan, J. P. (2017). Lower Crustal Strength Controls on Melting and Serpentinization at Magma-Poor Margins: Potential Implications for the South Atlantic. *Geochemistry, Geophysics, Geosystems*, *18*(12), 4538–4557. https://doi.org/10.1002/2017GC007212

Royden, L., & Keen, C. E. (1980). Rifting process and thermal evolution of the continental margin of Eastern Canada determined from subsidence curves. *Earth and Planetary Science Letters*, *51*(2), 343–361. https://doi.org/10.1016/0012-821X(80)90216-2

Ruh, J. B., Tokle, L., & Behr, W. M. (2022). Grain-size-evolution controls on lithospheric weakening during continental rifting. *Nature Geoscience*, *15*(7), 585–590. https://doi.org/10.1038/s41561-022-00964-9

Ryan, W. B. F., Carbotte, S. M., Coplan, J. O., O'Hara, S., Melkonian, A., Arko, R., Weissel, R. A., Ferrini, V., Goodwillie, A., Nitsche, F., Bonczkowski, J., & Zemsky, R. (2009). Global multi-resolution topography synthesis. *Geochemistry, Geophysics, Geosystems*. https://doi.org/10.1029/2008GC002332

Sakai, T., Belyakov, A., Kaibyshev, R., Miura, H., & Jonas, J. J. (2014). Dynamic and post-dynamic recrystallization under hot, cold and severe plastic deformation conditions. *Progress in Materials Science*, *60*(1), 130–207. https://doi.org/10.1016/J.PMATSCI.2013.09.002

Schaltegger, U., Desmurs, L., Manatschal, G., Muntener, O., Meier, M., Frank, M., & Bernoulli, D. (2002). The transition from rifting to sea-floor spreading within a magma-poor rifted margin: field and isotopic constraints. *Terra Nova*, *14*(3), 156–162. https://doi.org/10.1046/j.1365-3121.2002.00406.x

Schmeling, H. (2010). Dynamic models of continental rifting with melt generation. *Tectonophysics*, *480*(1–4), 33–47. https://doi.org/10.1016/j.tecto.2009.09.005

Searle, R. (2013). *Mid-Ocean Ridges*. Cambridge University Press. https://doi.org/10.1017/CBO9781139084260

Seymour, N. M., Strickland, E. D., Singleton, J. S., Stockli, D. F., & Wong, M. S. (2018). Laramide subduction and metamorphism of the Orocopia Schist, northern Plomosa Mountains, west-central Arizona: Insights from zircon U-Pb geochronology. *Geology*, *46*(10), 847–850. https://doi.org/10.1130/G45059.1

Shuck, B. D., Van Avendonk, H. J. A., & Bécel, A. (2019). The role of mantle melts in the transition from rifting to seafloor spreading offshore eastern North America. *Earth and Planetary Science Letters*, *525*, 115756. https://doi.org/10.1016/j.epsl.2019.115756

Skelton, A., Whitmarsh, R., Arghe, F., Crill, P., & Koyi, H. (2005). Constraining the rate and extent of mantle serpentinization from seismic and petrological data: implications for chemosynthesis and tectonic processes. *Geofluids*, *5*(3), 153–164. https://doi.org/10.1111/ j.1468-8123.2005.00111.x

Spadea, P., Zanetti, A., & Vannucci, R. (2003). Mineral chemistry of ultramafic massifs in the Southern Uralides orogenic belt (Russia) and the petrogenesis of the Lower Palaeozoic ophiolites of the Uralian Ocean. *Geological Society, London, Special Publications*, *218*(1), 567–596. https://doi.org/10.1144/GSL.SP.2003.218.01.29

Speciale, P. A., Behr, W. M., Hirth, G., & Tokle, L. (2020). Rates of Olivine Grain Growth During Dynamic Recrystallization and Postdeformation Annealing. *Journal of Geophysical Research: Solid Earth*, *125*(11). https://doi.org/10.1029/2020JB020415

Strickland, E. D., Singleton, J. S., & Haxel, G. B. (2018). Orocopia Schist in the northern Plomosa Mountains, west-central Arizona: A Laramide subduction complex exhumed in a Miocene metamorphic core complex. *Lithosphere*, *10*(6), 723–742. https://doi.org/10.1130/ L742.1

Svartman Dias, A. E., Hayman, N. W., & Lavier, L. L. (2016). Thinning factor distributions viewed through numerical models of continental extension. *Tectonics*, *35*(12), 3050–3069. https://doi.org/10.1002/2016TC004266

Svartman Dias, A. E., Lavier, L. L., & Hayman, N. W. (2015). Conjugate rifted margins width and asymmetry: The interplay between lithospheric strength and thermomechanical processes. *Journal of Geophysical Research: Solid Earth*, *120*(12), 8672–8700. https://doi.org/ 10.1002/2015JB012074

Theunissen, T., & Huismans, R. S. (2022). Mantle exhumation at magma-poor rifted margins controlled by frictional shear zones. *Nature Communications*, *13*(1), 1634. https://doi.org/ 10.1038/s41467-022-29058-1

Tucholke, B. E., Lin, J., & Kleinrock, M. C. (1998). Megamullions and mullion structure defining oceanic metamorphic core complexes on the Mid-Atlantic Ridge. *Journal of Geophysical Research: Solid Earth*, *103*(5), 9857–9866. https://doi.org/10.1029/98jb00167

Tugend, J., Gillard, M., Manatschal, G., Nirrengarten, M., Harkin, C., Epin, M.-E., Sauter, D., Autin, J., Kusznir, N., & McDermott, K. (2018). Reappraisal of the magma-rich versus magma-poor rifted margin archetypes. *Geological Society, London, Special Publications*, SP476.9. https://doi.org/10.1144/sp476.9

Tullis, J., & Yund, R. A. (1985). Dynamic recrystallization of feldspar: A mechanism for ductile shear zone formation. *Geology*, *13*(4), 238. https://doi.org 10.1130/0091-7613(1985)13<238:DROFAM>2.0.CO;2

van Avendonk, H. J. A., Holbrook, W. S., Nunes, G. T., Shillington, D. J., Tucholke, B. E., Louden, K. E., Larsen, H. C., & Hopper, J. R. (2006). Seismic velocity structure of the rifted margin of the eastern Grand Banks of Newfoundland, Canada. *Journal of Geophysical Research: Solid Earth*, *111*(11). https://doi.org/10.1029/2005JB004156

van Avendonk, H. J. A., Lavier, L. L., Shillington, D. J., & Manatschal, G. (2009). Extension of continental crust at the margin of the eastern Grand Banks, Newfoundland. *Tectonophysics*, *468*(1–4), 131–148. https://doi.org/10.1016/j.tecto.2008.05.030

Van der Wal, D., Chopra, P., Drury, M., & Gerald, J. F. (1993). Relationships between dynamically recrystallized grain size and deformation conditions in experimentally deformed olivine rocks. *Geophysical Research Letters*, *20*(14), 1479–1482. https://doi.org/ 10.1029/93GL01382

Vieira Duarte, J. F., Kaczmarek, M. A., Vonlanthen, P., Putlitz, B., & Müntener, O. (2020). Hydration of a mantle shear zone beyond serpentine stability: a possible link to microseismicity along ultraslow spreading ridges?. *Journal of Geophysical Research: Solid Earth*, *125*(10), e2020JB019509.

Warren, J. M., & Hirth, G. (2006). Grain size sensitive deformation mechanisms in naturally deformed peridotites. *Earth and Planetary Science Letters*, *248*(1–2), 438–450. https://doi.org/10.1016/J.EPSL.2006.06.006

Whitmarsh, R. B., Manatschal, G., & Minshull, T. A. (2001). Evolution of magma-poor continental margins from rifting to seafloor spreading. *Nature*, *413*(6852), 150–154. https://doi.org/10.1038/35093085

Zhao, M., Qiu, X., Li, J., Sauter, D., Ruan, A., Chen, J., Cannat, M., Singh, S., Zhang, J., Wu, Z., & Niu, X. (2013). Three-dimensional seismic structure of the Dragon Flag oceanic core complex at the ultraslow spreading Southwest Indian Ridge (49°39′E). *Geochemistry, Geophysics, Geosystems*, *14*(10), 4544–4563. https://doi.org/10.1002/ggge.20264